Interpretation of electromagnetic modes in the sub-TAE frequency range in JET plasmas with elevated monotonic q-profiles

N. Fil[1,2]‡, S.E. Sharapov[1], M. Fitzgerald[1], G.J. Choi[3], Z. Lin[3], R.A. Tinguely[2], H.J.C. Oliver[1], K.G. McClements[1], P.G. Puglia[4], R.J. Dumont[5], M. Porkolab[2], J. Mailloux[1], E. Joffrin[5], and JET Contributors*

[1] UKAEA-CCFE, Culham Science Centre, Abingdon, Oxon, OX14 3DB, UK

[2] Plasma Science and Fusion Center, Massachusetts Institute of Technology, Cambridge, MA 02139, USA

[3] Department of Physics and Astronomy, University of California, Irvine, CA 92697, USA

[4] Swiss Plasma Center, Ecole Polytechnique Fédérale de Lausanne, CH-1015 Lausanne, Switzerland

[5] CEA, IRFM, F-13108 Saint-Paul-lez-Durance, France

* See the author list of 'Overview of JET results for optimising ITER operation' by J. Mailloux *et al* to be published in *Nucl. Fusion* Special issue: Overview and Summary Papers from the 28th Fusion Energy Conference (Nice, France, 10-15 May 2021

Abstract. Recent JET Deuterium experiments with an advanced tokamak scenario using an internal transport barrier (ITB) have been performed to clearly observe destabilised toroidicity-induced Alfvén eigenmodes (TAEs) by fast ions; interestingly, these also exhibit unstable electromagnetic (EM) perturbations in the sub-TAE frequency range. We identify such EM perturbations to be beta-induced ion temperature gradient (BTG) eigenmodes and not beta-induced Alfvén eigenmodes (BAE) nor beta-induced Alfvén acoustic eigenmodes (BAAE) which are often unstable in such high-beta plasmas with high power neutral beam injection (NBI). The BTG modes are the most unstable modes due to the high thermal ion temperature gradient related to the ITB, high thermal ion temperature compared to thermal electron temperature (high T_i/T_e), and a high ion beta regime. BTG mode experimental characteristics match analytical theory, i.e. location in the vicinity of a rational magnetic surface with a low magnetic shear, mode frequency scaling with the ion diamagnetic frequency (ω_i^*), and a coupling among Alfvén and drift waves. We also perform linear gyrokinetic simulations with validated plasma profiles and equilibrium, and find a mode kinetically driven by thermal ions with similar characteristics as the experimental BTG modes.

Keywords: Alfvén-drift eigenmodes, Stability, Ion temperature gradient, Ion Landau drive/damping.

‡ Author to whom correspondence should be addressed: nicolas.fil@ukaea.uk

1. Introduction

JET Deuterium experiments aiming to develop an advanced tokamak scenario with an internal transport barrier (ITB) to observe alpha driven toroidicity-induced Alfvén eigenmodes (TAEs) [1] in Deuterium-Tritium (DT) plasmas have been performed with an elevated monotonic safety factor (q) profile with an extended central region of low positive shear, high plasma beta (β) regime, high core thermal ion temperature compared to the thermal electron one (core $T_i > 2 * T_e$) and high power of neutral beam injection (NBI). Such a high performance ITB scenario allows the core plasma region within the radius of the ITB to reach high thermal ion temperature with a steep radial gradient. It is also found that the ITB formation led to an increase of the thermonuclear contribution to the neutron rate (R_{NT}) [1]. Demonstrating alpha particle drive of Alfvénic instabilities in the forthcoming JET DT phase is key for our understanding of the underlying physics and for the success of future tokamak operation.

During those experiments we not only observed unstable TAEs - driven by ion cyclotron resonance heating (ICRH) fast ions in the absence of DT mixture as fuel - but also electromagnetic (EM) perturbations living in a frequency range below the TAEs which is often associated with the beta-induced gap created by the coupling between acoustic and Alfvén waves. Beta-induced eigenmodes are heavily studied with both experimental and theoretical analyses since they are often considered a source of additional transport of thermal plasma and fast ions, detrimental for current and future fusion devices. Basic physics of such eigenmodes can be found in [2]. In this work we focus on three main candidates for the observed EM perturbations: beta-induced Alfvén eigenmodes (BAE) [3, 4], beta-induced Alfvén acoustic eigenmodes (BAAE) [5] and beta-induced ion temperature gradient eigenmodes (BTG) [6]. The BTG mode is an electromagnetic analogue to the well-known *electrostatic* ion temperature gradient (ITG) instability [7, 8]. It is worth mentioning a parallel theory to BTG modes by [9–11] studying ion temperature gradient driven Alfvén eigenmodes (AITG). Such instabilities describe the coupling between two branches of the shear Alfvén wave: the BAE and the kinetic ballooning modes (KBM) [12] branches. In [11] the authors demonstrate the existence of AITG eigenmodes by including the finite ion Larmor radius (FLR) and finite drift-orbit width (FOW) effects. While this paper does not focus on comparing the BTG and AITG approaches, one can say that they agree on a few conditions of BTG/AITG mode existence such as a positive relative ion temperature gradient, a low magnetic shear and a strong thermal ion temperature gradient (∇T_i). An important distinction, BTG mode theory has a well-defined analytical criterion on ion beta which needs to be higher than a critical threshold ($\beta_{ion} > \beta_{ic}$). AITG mode theory demonstrates a strong dependence of the AITG mode real frequency with a factor α ($= -Rq^2 \frac{\mathrm{d}\beta}{\mathrm{d}r}$, where R is the major radius of the tokamak), i.e. with the safety factor and plasma beta. This factor α is then compared with the marginal stability boundary of ideal magnetohydrodynamic (MHD) ballooning modes ($\alpha_{crit}(\beta_{crit})$) [13]; AITG mode exists when $\beta > \beta_{AITG}$ with $\beta_{AITG} \lesssim 0.4 - 0.5\beta_{crit}$ [11]. The AITG mode real frequency scales with ω_i^* and increases when

α decreases. AITG modes are also predicted to be driven by the thermal ion temperature gradient and be enhanced when β_i increases. These last two criteria are consistent with the BTG mode theory. For the purpose of this work - to understand the nature and characteristics of the observed EM perturbations and study if such modes can be predicted by analytical theory and reproduced by numerical tools - we then consider the BTG and AITG theories to agree qualitatively on the criteria of existence of beta-induced ion temperature gradient driven eigenmodes, so we focus on BTG mode theory.

Section 2 presents the experimental evidence leading us to consider the EM perturbations to be unstable BTG modes. In Section 3 we find a good agreement between BTG mode analytical theory and experimental observations. The modeling effort to find such BTG modes using linear gyrokinetic simulations with a realistic JET geometry and validated equilibrium and plasma profiles is presented in Section 4. Finally a summary is given in Section 5.

2. Experimental observations

2.1. JET pulse 92054

To study sub-TAE modes we choose JET pulse (JPN) 92054 since it displays clear unstable electromagnetic perturbations below the TAE frequency range as one can see in Fig. 1a. For this pulse and time interval the characteristic TAE frequency in the plasma frame was $f_{TAE} \in [90, 102]\ kHz$. This frequency range is calculated using on-axis values for the densities and magnetic field in $f_{TAE} = V_A/4\pi qR$ with $V_A = B/\sqrt{\mu_0 \sum n_i m_i}$ the Alfvén speed where B is the toroidal magnetic field, $\sum n_i m_i$ the mass density of the plasma and μ_0 the vacuum permeability.

Another reason is that JPN 92054 has been extensively studied in [1] as part of JET experiments to observe alpha-driven instabilities so we are confident in the equilibrium reconstruction, experimental measurements, analysis as well as plasma profiles. The equilibrium are pressure constrained and use electron cyclotron emission (ECE) fast radiometer data correlated with MHD markers positions and neoclassical tearing mode (NTM) measurements [16] to confirm that the equilibrium q-profile is correct. To perform our TRANSP runs we took experimental measurements of thermal plasma parameters as inputs: for the electron density (n_e) we used measurements from high resolution Thomson scattering (HRTS) systems, the electron temperature (T_e) has been deduced from ECE and HRTS data, and the ion temperature (T_i) has been measured by charge exchange recombination spectroscopy (CXRS) of Neon X atoms, and X-Crystal spectroscopy (XCS). A good consistency has been found between the experimental neutron rate measurements and those assessed by the TRANSP code using the input set of measured plasma profiles. In Figure 5 in [1] one can see time traces of the auxiliary power, central electron and ion temperatures, toroidal rotation rate, electron density and neutron rate.

In this work we mainly focus on $6.4s$; Table 1 indicates the plasma parameters at that

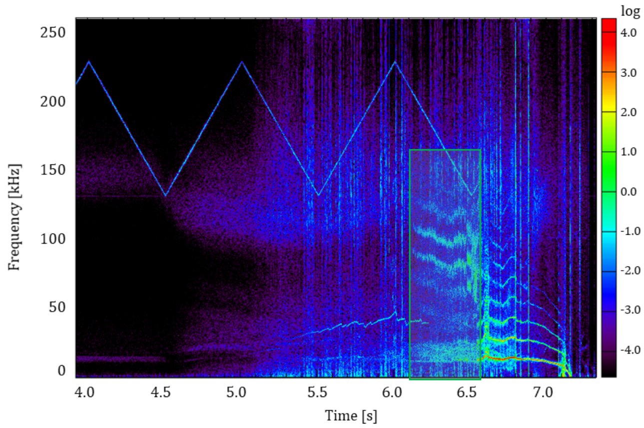

(a)

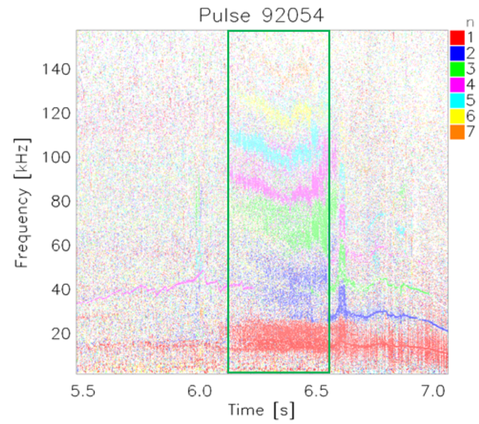

(b)

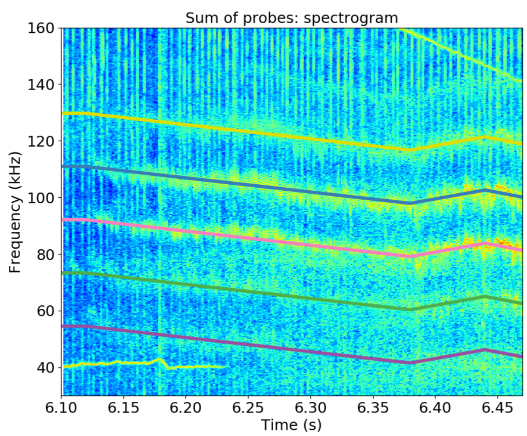

(c)

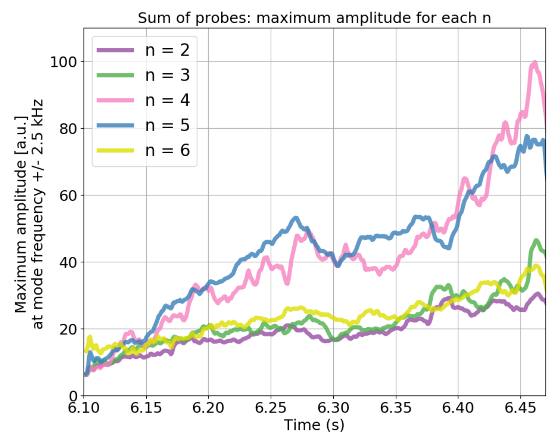

(d)

Figure 1: (a) Mirnov coil (H305) spectrogram of poloidal magnetic fluctuation frequency over time. (b) Mode analysis from a set of Mirnov coils analysing the relative phase shift of the fluctuations; the colours denote the toroidal mode numbers n. (c) Magnetic spectrogram considering all available magnetic Mirnov coils, zoomed in on the times of interest; the straight lines indicate the mean frequency (f_{mean}) used to filter and extract the amplitude information for each n. (d) Maximum amplitude in the frequency range $f_{mean} \pm 2.5kHz$ for each n in $[\![2, 6]\!]$. $n = 1$ and $n = 2$ modes' identification is difficult from the spectrogram. Note that the triangular shape signal on (a) is the JET TAE antenna magnetic perturbation scanning in frequency to resonate with stable plasma modes [14, 15].

time slice. q_0 indicates the safety factor at the magnetic axis; one can see the q-profile at $6.4s$ from EFIT reconstruction [17] in Fig. 7 where $q = 2$ is located at $\sqrt{\overline{\psi}} \sim 0.43$, with $\overline{\psi}$ the normalised toroidal flux. Note that ion density (n_i) and temperature (T_i) are quoted as ranges instead of a single value to highlight the uncertainties in the experimental measurements which are also reproduced in the TRANSP code [18] simulations; details on the TRANSP simulations can be found in section 6 from [1]. Due to the large error bars in T_i measurements, in this paper we consider two cases: (*low*-T_i) where T_i is chosen to be the lower range of error bars of CXRS measurements and (*high-T_i*) where T_i is taken to be the experimental value. By keeping measurement uncertainties we conserve a realistic picture of the experiments; how such uncertainties influence our results is discussed throughout the paper. Figure 2 shows the thermal plasma density and temperature profiles for our two cases with the mean between the two cases for the temperature profiles. One can see that the *high-T_i* case has a higher ion temperature gradient than the *low-T_i* case. Densities and electron temperature are similar for both cases.

Table 1: Plasma parameters for JET pulse 92054 at 6.4s. Data is from experimental measurements mapped in TRANSP code [18] and EFIT reconstruction [17].

Plasma parameters at 6.4s					
I_{p} (MA)	2.67	n_{e0} (10^{19} m^{-3})	5.43	B_0 (T)	3.44
R_{NT} (10^{16} s^{-1})	1.44	T_{e0} (keV)	5.4	q_0	1.86
P_{NBI} (MW)	25.1	n_{i0} (10^{19} m^{-3})	4.80-4.84	R_0 (m)	3.03
P_{ICRH} (MW)	0.00	T_{i0} (keV)	8.9-13.7	V_A (10^6 m.s^{-1})	7.06
Beta Toroidal					
$\beta_T(\%) = 3.67$ — $\beta_{ion}(\%) = 2.00$ — $\beta_{electron}(\%) = 0.95$ — $\beta_{beam}(\%) = 0.72$					

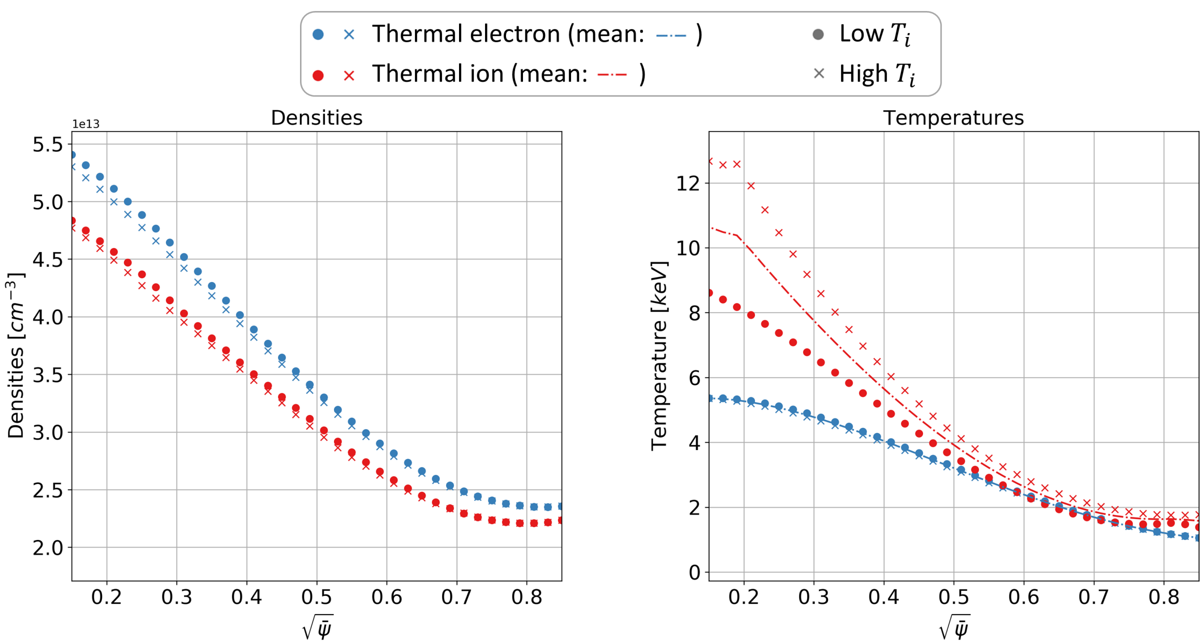

Figure 2: x-axis is the square root of the normalised toroidal flux ($\sqrt{\psi}$). TRANSP thermal plasma profiles: densities and temperatures. (*low-T_i*) is for T_i chosen to be the lower range of error bars of charge exchange recombination spectroscopy (CXRS) measurements ($T_{\mathrm{i0}} \sim 8.9keV$) and (*high-$T_i$*) where T_i is taken to be the experimental value ($T_{\mathrm{i0}} \sim 13.0keV$). The dashed line represents the mean between the two cases. Densities and electron temperature are similar for both cases.

Another important aspect of JPN 92054 is its high-β regime [19–22] with a normalised beta $\beta_N = \beta_T B_T a/I_P \sim 4.38[\% Tm/MA]$ at $t = 6.4s$ where β_T is the total toroidal beta in percent, B_T the toroidal field, a is the horizontal minor radius in meters and I_p is the plasma current in MA (see Table 1 for actual values). Such a regime gives conditions for beta-induced modes to exist such as BAE, BAAE and BTG, candidates for our modes of interest.

JPN 92054 also features a clear internal transport barrier (ITB) associated with the $q = 2$ magnetic surface; both electron and ion temperature profiles exhibit high gradients, ∇T_e and ∇T_i respectively (see section 3 in [1]). The onset time of the modes of interest is near the ITB observation leading us to consider that such temperature gradients could be the driving source of these EM modes; this would mean that we are observing unstable BTG modes. The following subsections - Section 2.2 and Section 2.3 - confirm this conjecture.

2.2. Electromagnetic perturbation evidence

Figure 1a represents the magnetic perturbations of the plasma measured at the wall by Mirnov pick-up coils. One can see modes being destabilised between 6.1 and 6.5s from ~ 10 to $\sim 140kHz$ in the lab frame (within the green square). On Fig. 1b the toroidal mode numbers (n) are obtained by making a time-windowed Fourier decomposition of the signals of a set of toroidally separated Mirnov coils and analysing the relative phase shift of the fluctuations; this technique allows to differentiate positive and negative n. $n = 1$ and $n = 2$ modes' identification is difficult from the spectrogram so our study will mainly focus on $n \in [\![3, 6]\!]$ modes. We cannot extract radial information from Magnetic signals, but this information is obtainable by analysing interferometry, Soft X-Ray (SXR) and/or reflectometry measurements on JET. Note that on JET, the reflectometer (KG8C) has the highest radial resolution followed by SXR (KJ5) and then the far infrared interferometer (KG1V). Unfortunately JET's frequency-hopping reflectometers had a limited operational range during this JPN 92054 since only the W band was available at the time, but we can still confirm that the modes appear near $R \sim 3.42m$ while we scan inward. Determination of the mode's full radial location was unfortunately not achievable due to limitations of the diagnostic: the scan was limited to $R(m) \in [3.35, 3.85]$ then the modes were only detected within $R(m) \in [3.35, 3.42]$ or $\sqrt{\psi} \in [0.41, 0.49]$. Interferometry and SXR also acquired data which show similar perturbations in time and frequencies as the Mirnov coils. Note that both SXR and interferometer diagnostics on JET provide line-integrated data with rather limited radial resolution. The interferometer on JET has four lines of sight, two of them close to the magnetic axis and the two others at the plasma edge (see Figure 1 from [23]); only the two channels looking at the plasma core measured density fluctuations related to the modes of interest. These two channels are on a different side of the magnetic axis, and comparison of the modes signals from these positions shows that the modes are neither ballooning nor anti-ballooning; modes with a single dominant poloidal mode number m are good candidates. SXR has seventeen lines of sights from bottom to top of the plasma: the mode location can be crudely estimated to be between $R[m] \in [2.2, 3.8]$ or $\sqrt{\psi} \in [0, 0.8]$.

Another method to estimate the modes' location is by comparing the mode frequencies in the plasma frame (f_{plasma}) with the ones measured in the lab frame (f_{lab}) by adding the Doppler shift from the plasma rotation frequency (f_{rot}). To evaluate f_{rot}, we used charge exchange recombination spectroscopy (CXRS) measurements. Only the toroidal rotation (f_{tor}) has been used, considering the poloidal rotation negligible, yet adding some uncertainties to f_{rot}. We then use $f_{lab} = f_{plasma} + nf_{tor}$. At $q = 2$: $f_{tor|q=2} \sim 15.38\ kHz$. The experimental uncertainties are higher near the magnetic axis than at the plasma edge, the sum of squared differences (SSD) divided by the number of data points is $\pm\ 0.18kHz$. The plasma frame frequencies can be estimated with a linear analytical dispersion relation depending on the nature of the mode. For such EM modes in the sub-TAE frequency range in a high-β plasma, good candidates are BTG, BAE and BAAE.

BTG mode frequency scales with the ion diamagnetic drift frequency (ω_i^*), reported by [24] as

$$\omega_j^* = -\frac{m}{r}\,\frac{m_j}{\omega_{cj}}\,\frac{T_j}{P_j}\,\frac{dP_j}{dr} = -\frac{nq}{r}\,\frac{c}{Z_j\ e\ B}\,\frac{T_j}{P_j}\,\frac{dP_j}{dr} \qquad (1)$$
$$with\ j = i\ for\ ions\ and\ e\ for\ electrons.$$

where m is the poloidal mode number ($m = nq$), r is the minor radius, c the speed of light, T_j the species temperature, Z_j the species charge state, e the elementary charge, B the magnetic field on-axis, ω_{cj} is the species gyrofrequency ($\omega_{cj} = Z_j eB/c\, m_j$), P_j the species pressure and dP_j/dr the species pressure radial gradient.

The frequency of BAE modes follows the frequency of geodesic acoustic modes (GAMs) [25] which is calculated with

$$f_{GAM}^2 = \frac{1}{4\pi^2}\left[\frac{2}{m_i R^2}\left(T_e + \frac{7}{4}T_i\right)\left(1 + \frac{1}{2q^2}\right)\right]\frac{2}{\kappa^2 + 1} \qquad (2)$$

where κ is the plasma flux surface elongation.

The nature of BAAE mode and its frequency in the plasma frame are still discussed, and one can find a clear review of BAAE observations and interpretations in [26]. For the purpose of this work we focus on the BAAE described by MHD [27] which has a frequency following the GAM frequency but shifted downwards by the toroidal inertia enhancement factor $1/(1+2q^2)$,

$$f_{BAAE}{}^2_{|MHD} = \frac{1}{1 + 2q^2}\ f_{GAM}^2 \qquad (3)$$

We also note recent DIII-D experimental "BAAE" [27] - now called low-frequency modes (LFM) [26] - which scale with diamagnetic drift frequencies with a strong dependence on electrons' parameters, especially with T_e or its gradient (∇T_e) that needs to be large for this instability to occur. Such LFMs in DIII-D has been identify using linear gyrokinetic simulations with the Gyrokinetic Toroidal Code (GTC) [28] as an interchange-like electromagnetic mode excited by non-resonant drive of thermal plasma pressure gradients and has a frequency on the order of the ion diamagnetic frequency (ω_i^*) [29].

Figure 3 represents the characteristic frequencies of the beta-induced modes previously mentioned. BAE and BAAE plasma frame frequencies do not depend on toroidal mode number (n) while the ion diamagnetic frequency does. We choose to only use $n \in \{1, 4, 6\}$ for ω_i^* not to overwhelm the figure. These frequencies are calculated using mean values of measured profiles mapped into TRANSP (see dashed line in Fig. 2) while error bars represent the experimental uncertainties of thermal plasma densities and temperatures reproduced in TRANSP profiles.

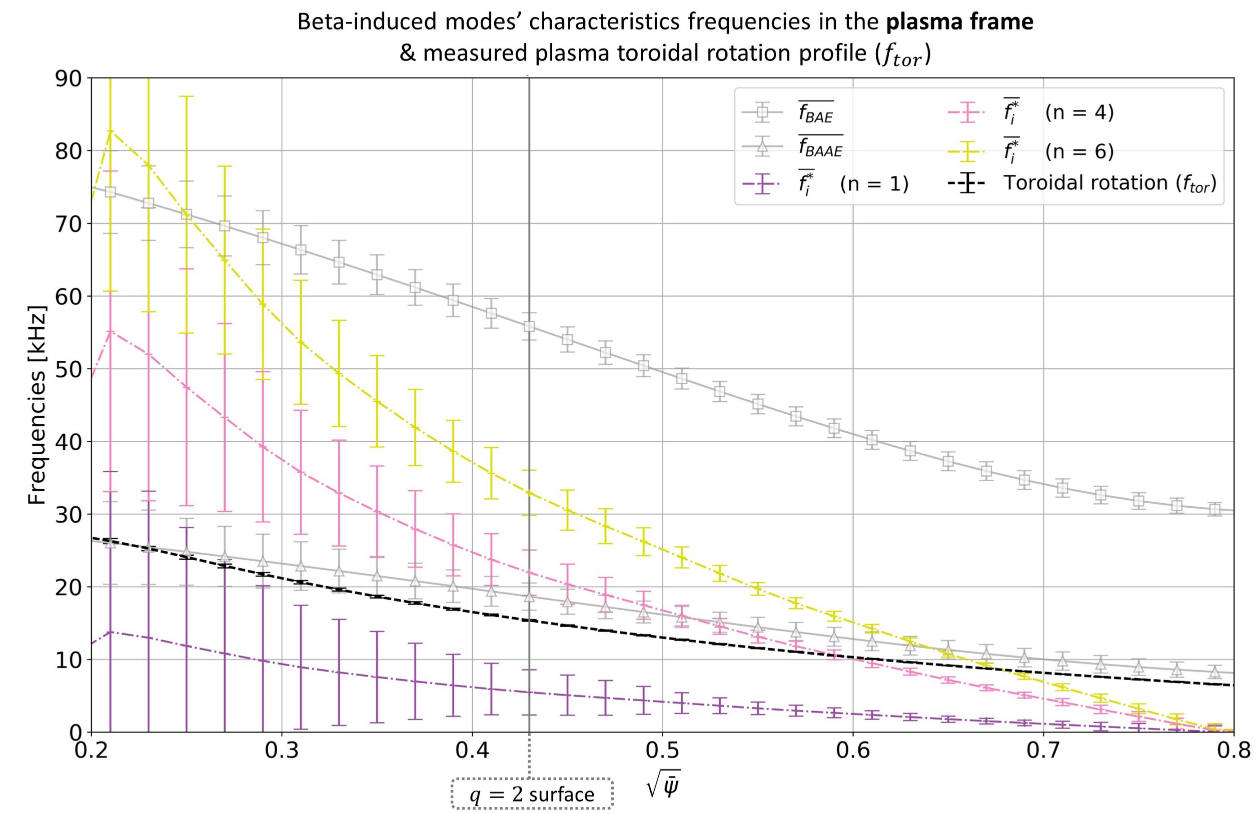

Figure 3: $\sqrt{\psi}$ the square root of the normalised toroidal flux. Plasma frame characteristic frequencies with ion diamagnetic frequency (f_i^*) for $n \in \{1, 4, 6\}$, BAE/GAM frequency (f_{BAE}) and BAAE frequency (f_{BAAE}). Toroidal plasma rotation (f_{tor}) profile from charge exchange recombination spectroscopy (CXRS) measurements represented with the black dashed line. At $q = 2$, $\omega^*_{i\,|n=4} \sim 21.9 \pm 3.1 kHz \sim 0.058 \pm 0.008[V_A/R_0]$, $f_{GAM} = f_{BAE} \sim 55.8 \pm 1.9 kHz \sim 0.148 \pm 0.005[V_A/R_0]$ and $f_{BAAE|MHD} \sim 18.7 \pm 0.6 kHz \sim 0.049 \pm 0.002[V_A/R_0]$.

To compare these frequencies with experimental measurements (Fig. 1b) we then applied the Doppler shift correction using the toroidal plasma rotation profile, i.e. $f_{lab} = f_{plasma} + nf_{tor}$. The frequencies in the lab frame are then compared with the frequency range for each n obtained from the time-windowed Fourier decomposition of the signals of a set of toroidally separated Mirnov coils. Figure 4 shows the best match with experiment which is for the ion diamagnetic frequencies; for $n \in [\![1, 6]\!]$ we plot $f_i^* + nf_{tor}$ with the experimental frequency ranges represented by the shaded horizontal areas, where colors match the respective single n values. Error bars for the frequencies in the lab frame also include the uncertainties from toroidal plasma rotation measurements. The BAE/GAM frequency is too high while the MHD BAAE frequency does not match experimental frequencies; when we add the plasma toroidal rotation term (nf_{tor}) to the BAAE frequency (Eq. (3)) then the non-dependence of $f_{BAAE|MHD}$ on the toroidal mode number leads to a mismatch between experimental frequency ranges and BAAE estimated lab frame frequencies. For $n \in \{1, 2, 3\}$ $f_{BAAE|MHD} + nf_{tor}$ is too low while for $n \in \{4, 5, 6\}$ it is too high.

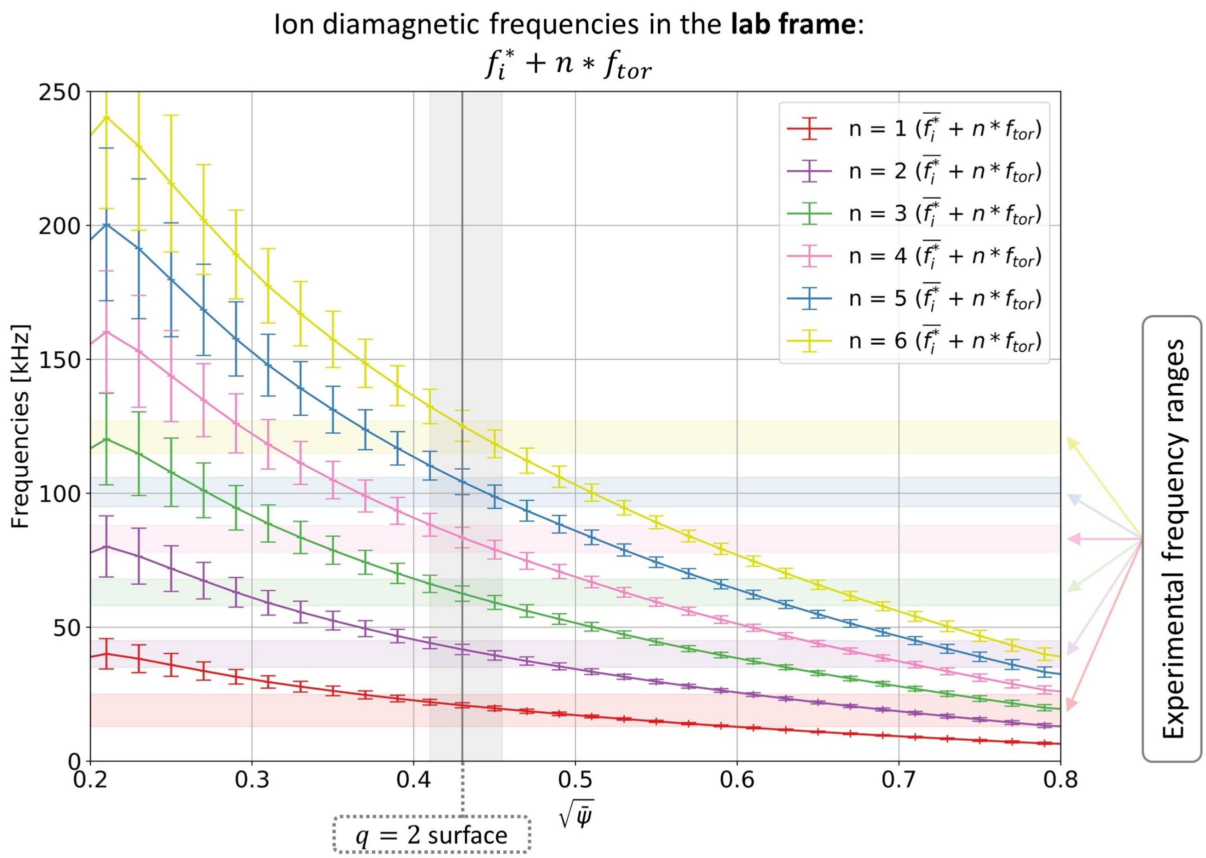

Figure 4: $\sqrt{\psi}$ the square root of the normalised toroidal flux. Ion diamagnetic frequencies (f_i^*) for $n \in [\![1, 6]\!]$ in the lab frame when Doppler shift is taken into account, i.e. $f_i^* + nf_{tor}$ with f_{tor} the toroidal plasma rotation from CXRS measurements. The shaded horizontal areas represent the experimental frequency range measured from the time-windowed Fourier decomposition of the signals of a toroidal set of Mirnov coils (see Fig. 1b). Note that the frequency ranges are large due to the very few number of coils available and signals' noise. Error bars represent the experimental uncertainties on thermal densities and temperatures as well as from toroidal plasma rotation measurements.

From this analysis, we can also estimate the modes' location to be around the $q = 2$ surface ($\sqrt{\psi} \in [0.41, 0.45]$) which is consistent with the ITB's formation when this magnetic surface appears (see Section 2.1). This is also consistent with the reflectometry, interferometry and SXR measurements reported above estimating the modes' location within $\sqrt{\psi} < 0.49$.

2.3. *Electromagnetic perturbation dependencies*

To get a better understanding of the nature of the destabilised electromagnetic modes we compared the temporal evolution of the mode frequency ($\in [6.1, 6.5]s$) with several plasma parameters: n_e, T_e, ∇T_e, n_i, T_i, ∇T_i, NBI fast ion density (n_{fi}) and temperature (T_{fi}), plasma pressure (p) and its gradient (p') and the Alfvén frequency on axis ($f_{A0} = V_{A0}/2\pi q_0 R = B_0/2\pi q_0 R\sqrt{\mu_0 \sum n_{i0} m_i}$) as well as with characteristic frequencies ω_i^*, f_{GAM} and $f_{BAAE|MHD}$. For each quantity we calculate the Pearson correlation coefficient [30] between its temporal evolution and the temporal evolution of the mode frequency. We performed this analysis at the following radial locations: on-axis (q_0) and at $q = 2, 9/4, 10/4, 11/4, 3$ rational surfaces. The best correlations are found at the $q = 2$ surface adding more confidence on the modes' location; they are reported in Table 2. The higher correlation coefficients are obtained with ∇T_i and ω_i^* indicating that the destabilised modes could be driven by the thermal ion temperature gradient, hence being BTG modes. This differs from the DIII-D experimental LFMs which need a large electron temperature (T_e) or its gradient (∇T_e) for instability. We also note a low correlation with $1/\sqrt{T_i}$ associated with ion sound scaling [31]; this indicates a weak coupling between the destabilised modes and the acoustic waves. A coupling of BAE or BAAE modes with ion sound waves is usually expected but not for BTG mode which does not strongly couple with acoustic waves.

Table 2: Pearson correlation coefficients [30] ($\in [-1, 1]$) between the temporal evolutions of the mode frequency and several plasma parameters. Note that such a coefficient measures the linear correlation between two sets of data; correlation coefficient of $+1$ implies that the relationship between the two set of data is perfectly described by a linear equation while a correlation coefficient of 0 implies that the two sets of data have no linear relationship. A positive correlation coefficient means that the two sets of data vary similarly (i.e. the mode frequency decreases/increases when the plasma parameter decreases/increases respectively), while a negative sign means that the two sets of data vary in opposite direction (i.e. the mode frequency decreases/increases when the plasma parameter increases/decreases respectively). For this analysis we then look for the highest positive correlation coefficient which is 0.98 obtained for ∇T_i followed by ω_i^* with 0.92.

$1/\sqrt{n_e}$	T_e	∇T_e	$1/\sqrt{n_i}$	$1/\sqrt{T_i}$	∇T_i	$1/\sqrt{n_{fi}}$	T_{fi}	$1/p$	p'	f_{A0}	ω_i^*	ω_e^*	f_{GAM}	f_{BAAE}
0.71	-0.56	0.85	0.77	0.18	0.98	-0.81	0.72	-0.65	0.09	-0.97	0.92	-0.93	0.87	0.05

The next section focuses on comparing our experimental results with the theoretical conditions for BTG mode to exist and become unstable.

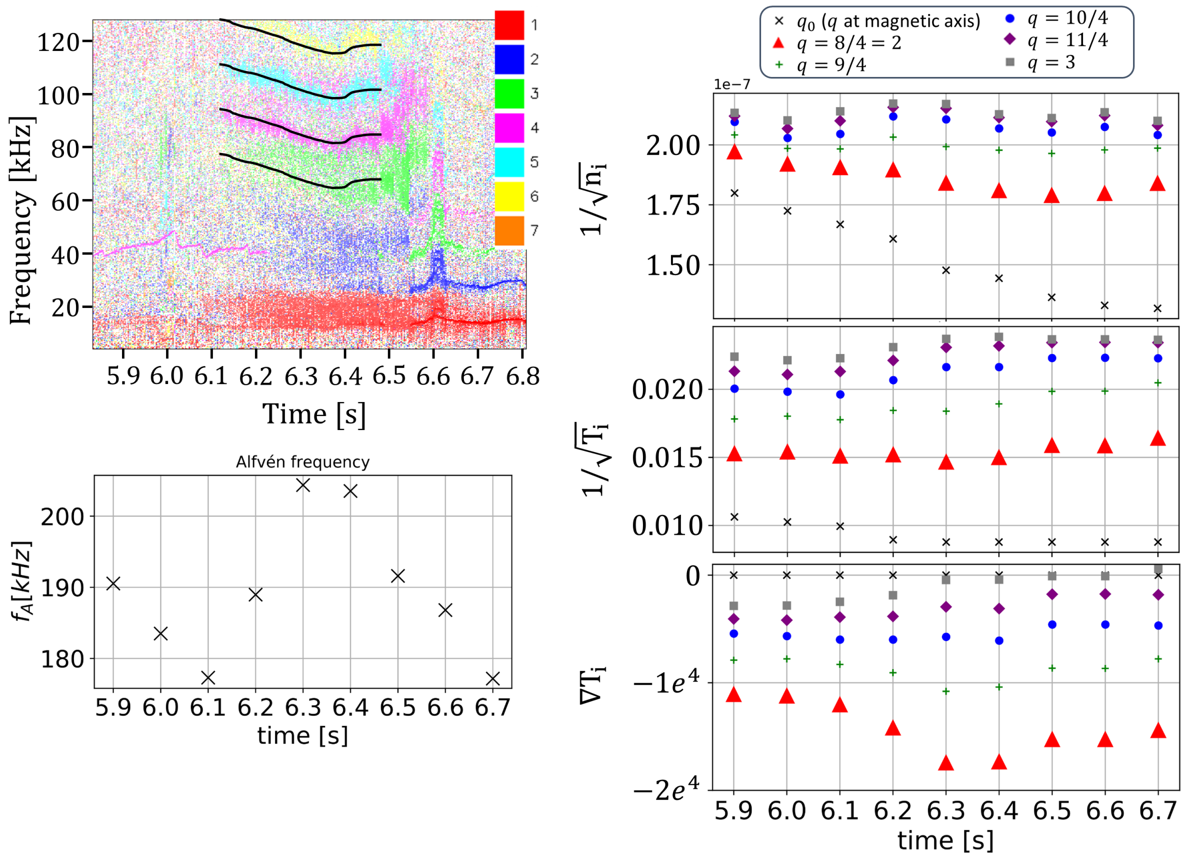

Figure 5: Time traces of the destabilised modes (top left) and of $1/\sqrt{n_i}$, $1/\sqrt{T_i}$ and ∇T_i for several rational surfaces (q_0 and $q = 2, 9/4, 10/4, 11/4, 3$) and of f_A on axis. The best correlations appears at the $q = 2$ surface (red triangles). ∇T_i and $1/\sqrt{n_i}$ temporal evolutions at $q = 2$ are strongly correlated with the EM perturbations' frequencies temporal evolution while $1/\sqrt{T_i}$ is weakly correlated. Note that the plasma density increases between $5.9s$ and $6.7s$ explaining the decrease of the on-axis Alfvén frequency (f_A); the increase of f_A between $6.1s$ to $6.3s$ is due to a decrease of q on-axis discussed at the end of Section 3.

3. Beta-induced ion temperature gradient driven eigenmodes

MHD and kinetic theories of BTG modes have been presented in [32] and [33] respectively; the purpose of this section is **not** to reproduce these analytical theories but to compare them with our experimental observations of JPN 92054 to confirm the correlation between the observed unstable EM perturbations between ~ 6.1 and $6.5s$ and the analytical BTG mode conditions of existence. BTG mode theories predict that above a certain ion beta threshold the drift effects due to the ion temperature gradient can lead to an appearance of unstable coupled Alfvén-drift eigenmodes, called BTG, which are localised in the vicinity of a rational magnetic surface ($q(r) = m/n$). Three well-defined conditions need to be fulfilled for BTG mode to exist. We first present these conditions for one time slice, $6.4s$, and for the *high-T_i* profile before focusing on other time slices, within and outside the times of interest

($[6.1, 6.5]s$).
The first BTG mode condition (i) is to have a positive relative ion temperature gradient (η_{ion}):

$$\frac{\partial \ln T_i}{\partial \ln n_i} = \eta_{ion} > 0 \tag{4}$$

Figure 6 shows η for thermal ions and electrons where one can see that condition (i) is verified for $\sqrt{\psi} \in [0.15, 0.90]$.

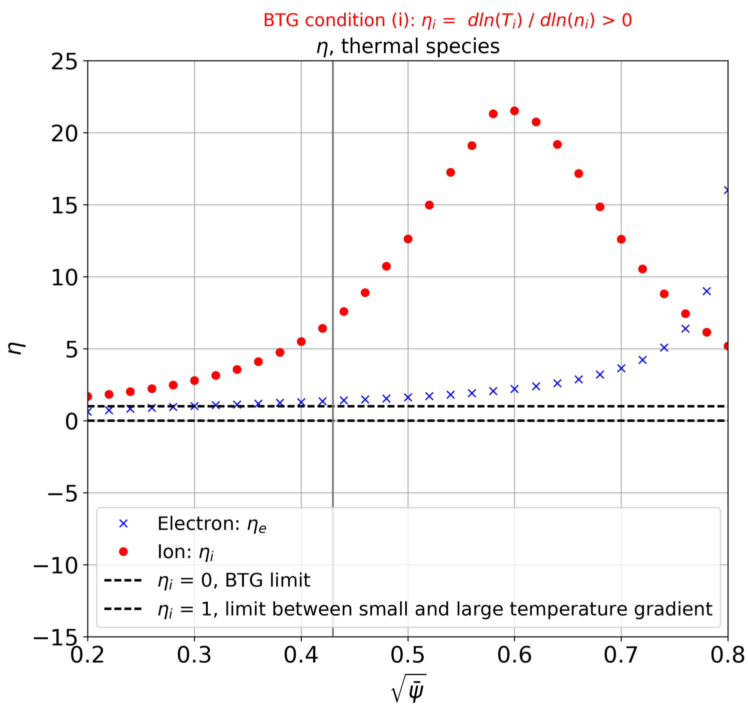

Figure 6: TRANSP thermal species relative temperature gradient profiles: $\eta = \partial \ln T / \partial \ln n$. For $\sqrt{\psi} \in [0.15, 0.90]$, BTG mode condition (i) ($\eta_{ion} > 0$) is verified. The vertical grey line indicates the position of the $q = 2$ surface.

The second BTG condition (ii) is that ion beta ($\beta_{ion} \cong 8\pi n_i T_i / B_0^2$) overcomes an analytical threshold value (β_{ic}) defined by

$$\beta_{ion} > \beta_{ic} = \frac{9}{2} \frac{q^2 S^2 L_{T_i}^2}{R^2} \tag{5}$$

where S is the magnetic shear, R the major radius of the tokamak and L_{T_i} is the characteristic scale length of the thermal ion temperature inhomogeneity ($L_{T_i} = T_i / \nabla T_i$). Figure 7 shows the ion beta (β_{ion}) versus the threshold value (β_{ic}): the condition (ii) is verified when $\sqrt{\psi} < 0.57$.

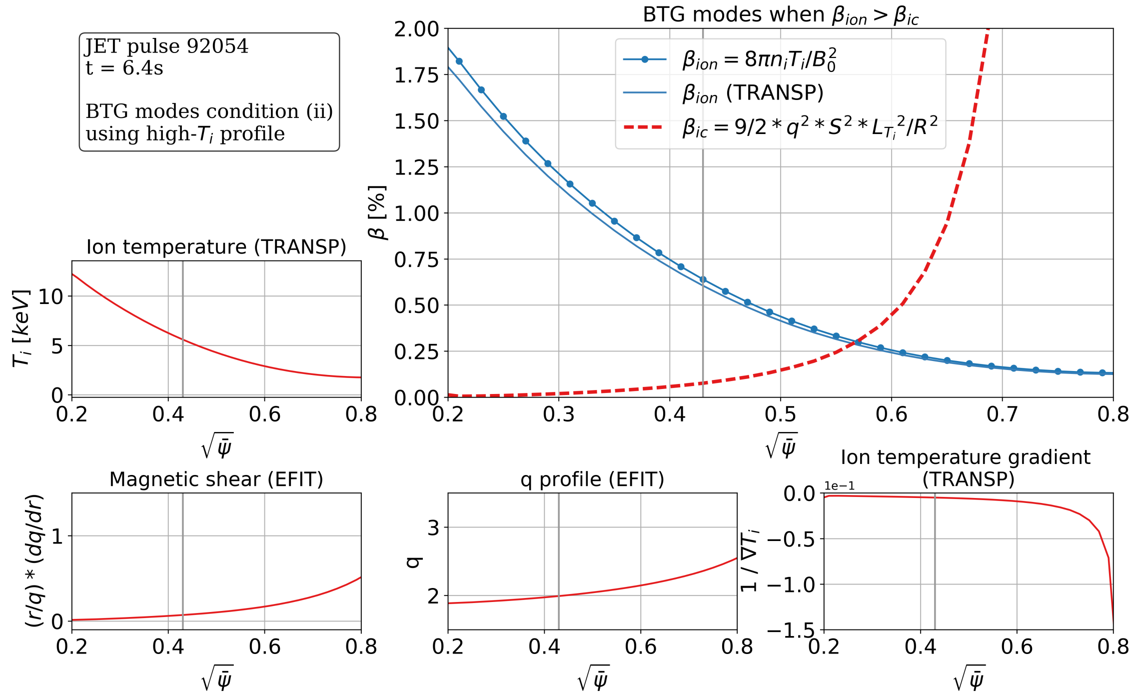

Figure 7: TRANSP ion temperature (T_i) and inverse ion temperature gradient ($1/\nabla T_i$) profiles with EFIT magnetic shear and q profiles are used to evaluate BTG mode condition (ii): $\beta_{ion} > \beta_{ic} = 9q^2 S^2 L_{T_i}^2 / 2R^2$. BTG mode could exist for $\sqrt{\bar{\psi}} < 0.57$. The vertical grey lines indicate the position of the $q = 2$ surface.

The third BTG condition (iii) means that the magnetic shear has to be small but not too low. When S is too low the magnetic well effect [34] becomes important leading to the suppression of the BTG eigenmodes. Condition (iii) is defined by

$$U_0 < 2 \text{ with} : U_0 = -\frac{8\pi r p_0^{'}}{S^2 B_0^2}(q^2 - 1) \tag{6}$$

where $p_0^{'}$ is the pressure gradient and B_0 toroidal magnetic field on-axis.

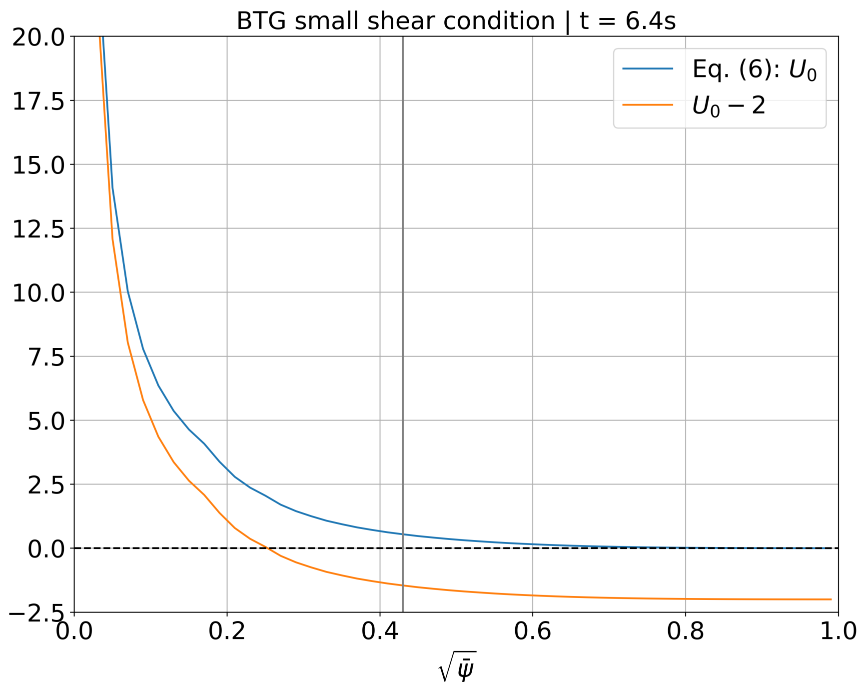

Figure 8: BTG mode condition (iii) on small magnetic shear ($U_0 < 2$) is verified for $\sqrt{\bar{\psi}} > 0.25$.

Figure 8 shows U_0 and $U_0 - 2$ calculated from equilibrium profiles where one can see that the condition (iii) is verified for $\sqrt{\bar{\psi}} \in [0.25, 1.0]$. Note that for $\sqrt{\bar{\psi}} < 0.25$ the magnetic shear is too low which is a condition when the BTG eigenmodes are suppressed [32].
If we now consider the three BTG conditions together (i) + (ii) + (iii), BTG mode could exist for $\sqrt{\bar{\psi}} \in [0.25, 0.57]$ which is consistent with Section 2.2, and this range includes the $q = 2$ magnetic surface. For the *low-*T_i case we have $\sqrt{\bar{\psi}} \in [0.25, 0.56]$, almost identical to the *high-*T_i case.

MHD [32] and kinetic [33] theories also present various cases for BTG eigenmode instabilities depending on the mode frequency (ω) compared with characteristic frequencies. We compare ω with (a) the ion transit frequency (ω_i) defined by

$$\omega_i = V_{Ti}/qR_0 \tag{7}$$

where V_{Ti} the ion thermal velocity ($V_{Ti} = \sqrt{T_i/m_i}$), with (b) the temperature-gradient ion drift frequency (ω^*_{Ti}) [11] defined by

$$\omega^*_{Ti} = \frac{nq}{r} \frac{c\ T_i}{Z_i\ e\ B} \frac{1}{L_{T_i}} \tag{8}$$

as well as with (c) the drift frequency (ω^*) which is defined by

$$\omega^* = k_y V^* = \frac{nq}{r} \frac{c\ T_i}{Z_i\ e\ B} \frac{1}{L_n} \tag{9}$$

where L_n is the characteristic scale length of the thermal plasma density inhomogeneity, and with (d) the frequency of the cylindrical Alfvén continuum spectrum [32], which represents the lower limit for a mode existing from the coupling among Alfvén, acoustic, and drift waves, i.e. BTG mode should have a frequency larger than such a limit:

$$\omega_{BTG} \geq V_A k_{\parallel}^{'} x^* \tag{10}$$

where $k_{\parallel}^{'} = dk_{\parallel}/dr$, $k_{\parallel}$ is the wave vector along the equilibrium magnetic field and x^* is the characteristic scale length of the coupled Alfvén and drift-acoustic waves ($x^* = (3/2)q^2\rho_i$, with ρ_i the ion Larmor radius).

Figure 9 shows these characteristic frequencies using $n = 4$; we find $\omega \cong \omega_i^* > \omega_i$. Such a condition, with $1 \ll \eta_{ion}$, in the kinetic BTG theory [33] means that the drive source of BTG modes comes from inverse ion Landau damping and the analytical dispersion relation reduces to $Re(\omega) = \omega_i^*$. Note that the condition for the inverse ion Landau damping is $Re(\omega) < 2 * \omega_i^*$ (see Eq. (7.15.3) in [7]).

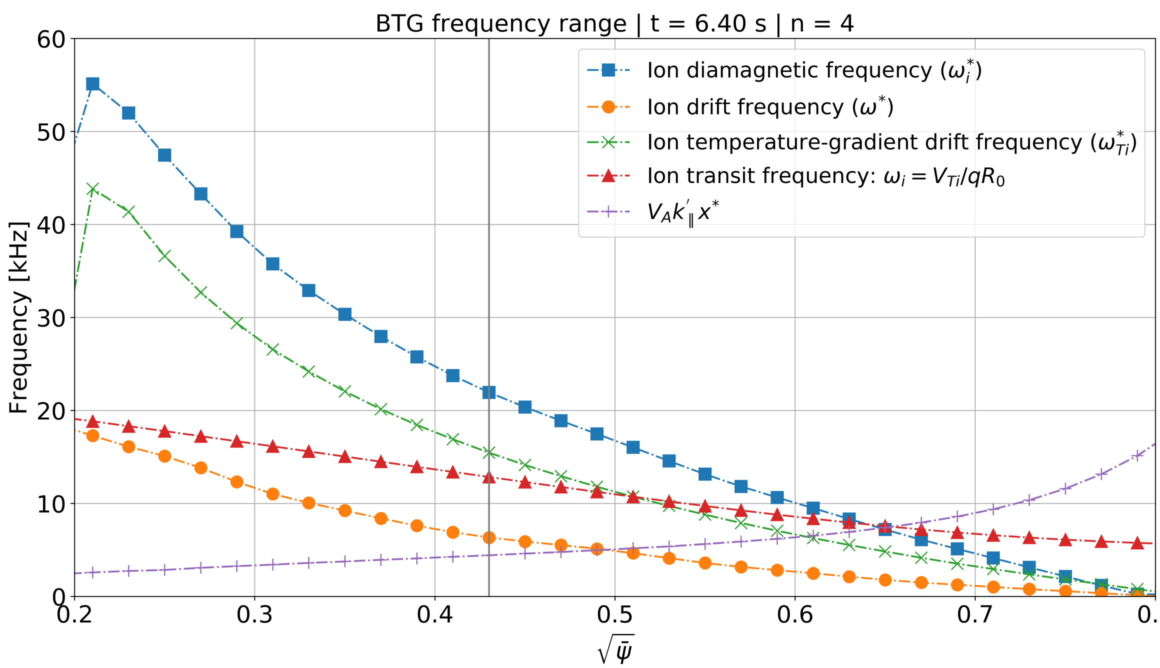

Figure 9: x-axis is the square root of the normalised toroidal flux ($\sqrt{\psi}$) and the $q = 2$ magnetic surface is indicated by the vertical grey line. Characteristic frequencies for BTG modes; at $q = 2$, from the highest to the lowest frequency, we have (blue square) the ion diamagnetic frequency (ω_i^*), (green cross) the ion temperature-gradient drift frequency (ω_{Ti}^*), (red triangle) the ion transit frequency (ω_i), (orange circle) the ion drift frequency (ω^*) and (purple +) the frequency of the cylindrical Alfvén continuum spectrum ($V_A k_{\parallel}^{'} x^*$).

BTG conditions are fullfilled at $t = 6.4s$; now we check if this is the case for other time slices to study the correlation between the observed unstable EM perturbations

($t(s) \in [6.1, 6.5]$) and analytical BTG modes. We present this analysis with yes(✓)/no(✗) flags, i.e. whether the BTG conditions are met or not for different time slices. Table 3 indicates time slices within and outside the time range of interest; when a BTG condition is met we indicate at which rational magnetic surface ($q = m/n$) in the corresponding cell. All three BTG conditions are met for the same magnetic surface for $t(s) \in [6.1, 6.6]$, before and after these times this is not the case. This shows a good correlation between the observed unstable EM perturbations and the analytical BTG modes.

Table 3: BTG conditions over time. "✓" means "yes" or that the condition is fullfilled while "✗" means it is not. Values in cells for BTG conditions are q values ($= m/n$). Good correlation is observed between unstable EM perturbations ($t(s) \in [6.1, 6.5]$) and analytical BTG modes. The equilibrium reconstruction is not accurate enough [1] for $t = 6.1s$ and $t = 6.2s$ with q-profiles too high to predict the $q = 2$ magnetic surface, while for $t = 6.6s$ the q-profile is too low. After $t = 6.7s$, no equilibrium reconstruction is available.

BTG conditions vs time — $n = 4$									
Time [s]	4.5-5.8	5.9-6.0	6.1	6.2	6.3	6.4	6.5	6.6	6.7
Unstable EM modes	✗	✗	✓	✓	✓	✓	✓	✗	✗
(i) $0 < \eta_{ion}$	11/4	10/4	10/4	9/4	8/4	8/4	8/4	8/4	8/4
(ii) $\beta_{ic} < \beta_{ion}$	✗	✗	10/4	9/4	8/4	8/4	8/4	8/4	8/4
(iii) $U_0 < 2$	11/4	10/4	10/4	9/4	8/4	8/4	8/4	8/4	9/4
$(i) + (ii) + (iii)$	✗	✗	10/4	9/4	8/4	8/4	8/4	8/4	✗
$q = 2$ (EFIT)	✗	✗	✗	✗	✓	✓	✓	✓	✓

At $t = 6.1s$ and $t = 6.2s$ we have higher q values than for the $t(s) \in [6.3, 6.6]$; this is due to the equilibrium reconstruction which is not accurate enough [1] with q-profiles too high to predict the $q = 2$ magnetic surface. The unstable EM perturbations disappear between $6.5s$ and $6.6s$ when NBI starts to decrease and the ion cyclotron resonance heating (ICRH) system is turned on for a safe plasma termination. After $t = 6.7s$, no equilibrium reconstruction is available. All these conditions add-on to the difficulty to have a high accuracy of the equilibrium reconstruction. Here we note that the experimental observation of unstable BTG modes could be used to constrain future equilibrium reconstructions to have the correct rational magnetic surfaces during the times of such instabilities, e.g. the $q = 2$ surface probably appears between $6.1s$ and $6.2s$ instead of between $6.2s$ and $6.3s$ predicted by EFIT code.

We have experimental evidence along with MHD and kinetic theories supporting the existence of BTG modes in JPN 92054 at $t(s) \in [6.1, 6.5]$. These modes are localised in the vicinity of the $q = 2$ magnetic surface with a frequency (ω) in the plasma frame such as $\omega \cong \omega_i^*$ with ω_i^* the ion diamagnetic frequency (at $t = 6.4s$ and $q = 2$, $\omega^*_{i\,|n=4} \sim 21.9 \pm 3.1kHz \sim 0.058 \pm 0.008[V_A/R_0]$). Kinetic BTG theory [33] states that the drive source of BTG modes comes from inverse ion Landau damping, and the analytical dispersion relation reduces to $Re(\omega) = \omega_i^*$. The following section, Section 4, is focused on performing MHD and gyrokinetic simulations using a realistic magnetic geometry and plasma profiles from JPN 92054 at 6.4s and comparing the results with both experimental observations and analytical theories.

4. Modelling

In Fig. 1d one can see that at $t = 6.4s$ the most unstable modes from experiment are $n = 4$ and $n = 5$. Simulations run for this study use a single n and several poloidal harmonics m; we decided to focus on $n = 4$. All frequencies from simulations are in the plasma frame ($f_{TAE_{plasma}}$); lab frame frequencies ($f_{TAE_{lab}}$) are estimated by adding the plasma toroidal rotation from the Doppler shift at the mode location ($f_{tor|mode\ location}$). Note that we do not take into account the experimental plasma poloidal rotation considered negligible at the mode location nor than the neoclassical flow effects from the simulation; therefore adding some uncertainties for the comparisons. Mode frequencies are either expressed in kHz or normalised by V_A/R_0, with $V_A[m/s]$ the Alfvén speed and $R_0[m]$ the radius of the magnetic axis.

We started by looking at the magnetohydrodynamic (MHD) picture using the linear ideal MHD code MISHKA-1 [35] (Section 4.1) since it is well-established on JET experiments for TAE studies; MISHKA-1 finds incompressible ideal solutions which is perfectly adapted to TAE studies, but it cannot capture beta-induced modes' physics hence not BAE, BAAE nor BTG modes. So in Section 4.2 we perform linear gyrokinetic simulations using the Gyrokinetic Toroidal Code (GTC) [28], a Particle-In-Cell (PIC) code, to study such beta-induced modes in JPN 92054. GTC has been successfully used to predict TAEs [36] and beta-induced modes and their stability with an analytical equilibrium [37] and more recently with a realistic experimental equilibrium and plasma profiles on DIII-D [29]. The gyrokinetic approach allows us to treat thermal ions and electrons independently, a necessity here to study the ion temperature gradient effect correctly. To demonstrate that we are running the GTC code in a correct manner for JET equilibrium and profiles we first perform a sanity check by comparing TAE predictions with both MISHKA-1 and GTC codes.

4.1. Magnetohydrodynamic simulations

4.1.1. MISHKA-1, incompressible MHD

We perform a frequency scan looking for modes with MISHKA-1, which solves the linearised ideal MHD equations in a JET toroidal geometry; it includes a vacuum region up to an ideally conducting wall. The JET equilibrium for JPN 92054 at 6.4s is calculated using the HELENA code [38] producing straight field line metric elements; the electron density profile from TRANSP is fitted with an 8^{th} order polynomial from which the coefficients are used to describe the density in MISHKA-1. As expected, we found some TAEs but no modes in the sub-TAE frequency range; Figure 10 presents a $n = 4, m = (8, 9)$ TAE mode at $\omega/\omega_0 \sim 0.241$

($f = 91.6kHz$) with a ballooning character being mainly localised on the outboard side as one can see on the poloidal plane plot.

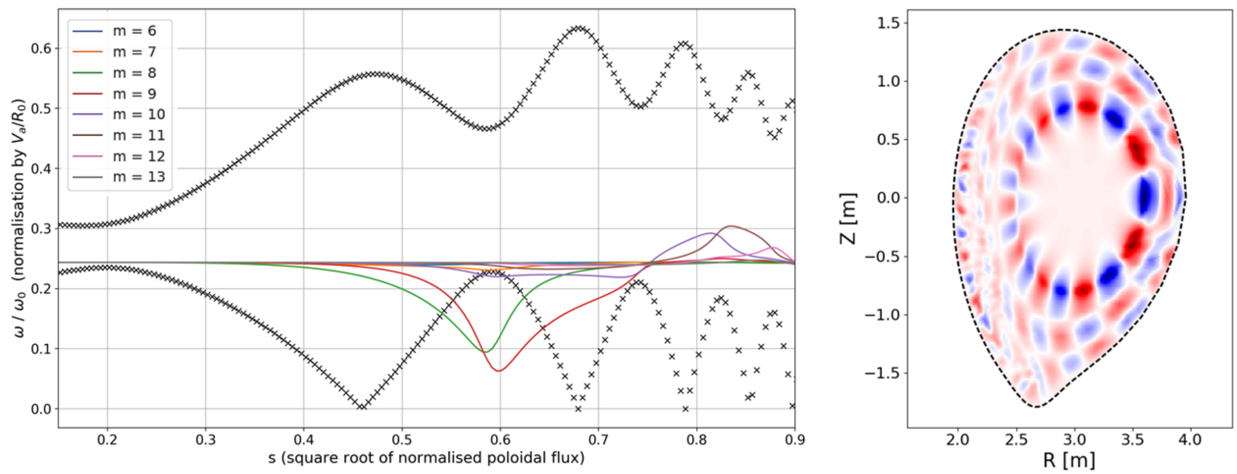

Figure 10: MISHKA-1 and CSCAS codes - (left) Alfvén continuum calculated by CSCAS code [39] of JET 92054 at 6.4s, solved for $n = 4$, $m \in [6, 26]$, 199 radial points ($\sqrt{\psi} \in [0.01, 1.0]$). Plotted on top of the Alfvén continuum is the real component of the electrostatic potential of the TAE mode at $\omega/\omega_0 \sim 0.241 \sim 91.6\ kHz$. Note the horizontal axis is the square root of the normalised **poloidal** flux. (right) is the real component of the electrostatic potential plotted on the poloidal plane. The black dashed line represents the last closed flux surface (LCFS).

4.1.2. GTC, TAE matching incompressible MHD

The same equilibrium and profiles used for MISHKA-1 simulations are used as inputs to GTC; this requires us to map the EFIT equilibrium to Boozer coordinates using a module from the ORBIT code [40] because GTC uses a field-aligned mesh in Boozer coordinates. Once this step is done, consistency of the equilibria is checked and validated to make sure simulations from different codes can indeed be compared. The GTC simulations presented in this paper are all linear electromagnetic global δf. The thermal electrons are treated as a massless fluid without kinetic effects. We neglect collisions and reduced our simulation domain to $\sqrt{\psi} \in [0.20, 0.80]$ to avoid any nonphysical effect from the lack of precision of TRANSP profiles at the edge or near the magnetic axis. We use 100x400x32 grids in radial, poloidal and parallel directions, respectively. To compare the MHD incompressible ideal solutions from MISHKA-1 (TAE mode in Fig. 10) with GTC prediction we need to only consider a single fluid of electrons keeping only the adiabatic terms in the linearized gyrokinetic equation. Figure 11 shows a marginally stable TAE found with GTC, which is the less damped mode in the simulation, since there is a negligible continuum damping of such a TAE; it has a spatial structure and frequency similar to the MISHKA-1 eigenmode giving confidence in using the GTC code on JPN 92054 with such equilibrium and plasma profiles.

With GTC we also study the TAE stability to see if it matches the experimental observations where no unstable TAE was observed during this pulse. We now need to take into account the thermal ion population which is treated gyrokinetically, and the thermal electron population is still simulated as a massless fluid but with kinetic effects from trapped electrons only [41]. The thermal ion population is described by an initial Maxwellian distribution. To respect quasi-neutrality, the ion density is identical to the electron one when we perform simulations without fast ions. The particle number per cell is 200. We obtain a non-perturbative calculation of thermal damping of $\gamma/\omega_{TAE} \sim -2.95\%$, which includes continuum, radiative and ion Landau damping mechanisms. We also performed a GTC simulation with NBI fast ions treated similar to the thermal ions: marginal difference in the total damping rate of the TAE was found. These predictions of a damped TAE are then consistent with experimental observations. Note that such a *stable* TAE is meant to be probed by the JET TAE antenna [14, 15], but unfortunately the TAE antenna scanned too high in frequency to resonate with this mode (see the antenna signal on Fig. 1a) with an antenna frequency at $155kHz$ (at $t = 6.4s$) compared to the simulated TAE mode frequency in the lab frame of $f_{TAE_{lab}} = f_{TAE_{plasma}} + nf_{tor|mode\ location} \sim 92 + 4 * 11 \sim 136kHz$.

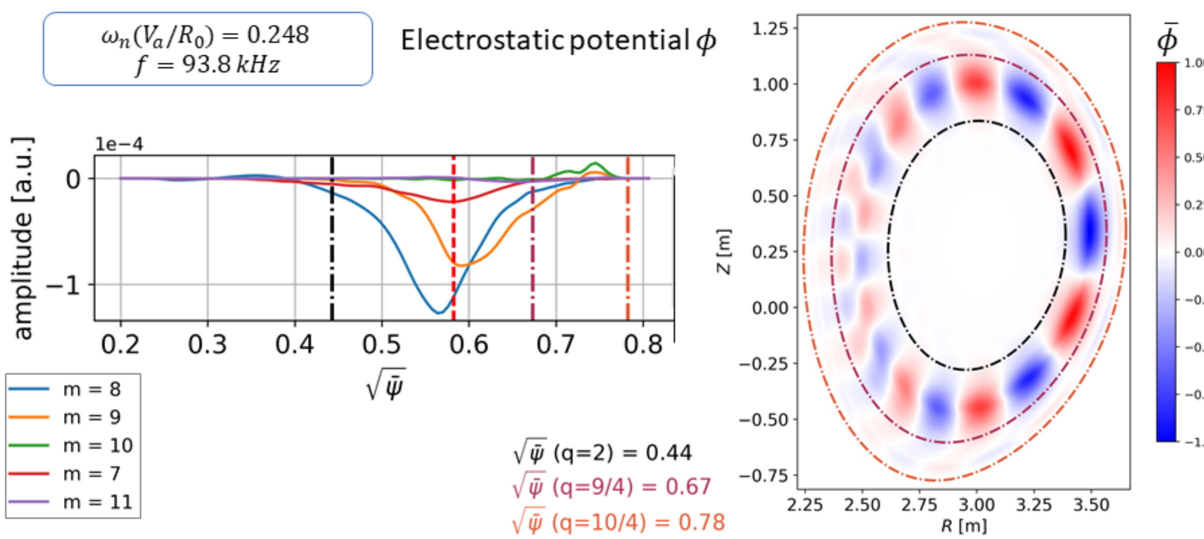

Figure 11: GTC - Real component of the electrostatic potential of the $n = 4$ TAE mode at $\omega/\omega_0 \sim 0.248$ plotted over the square root of the normalised toroidal flux (left) and poloidal plane (right). (left) The vertical red dashed line at $\sqrt{\psi} \sim 0.58$ indicates the position of the TAE gap from the coupling between the $m = 8$ and $m = 9$ poloidal harmonics. The mode spatial structure and frequency are similar to the MISHKA-1 eigenmode (Fig. 10).

4.2. Beta-induced modes in JPN 92054

Before presenting GTC simulations for modes with frequencies below the TAE frequency we first use the ALCON code [42] to solve the ideal MHD Alfvén continuum, i.e., Eq. (10) in [43] using a poloidal-spectral method described in Appendix A in [42]. Finite compressibility of the plasma is taken into account to predict MHD beta-induced gaps, the continuum is shown in Fig. 12. One can see several open gaps (TAE and BAAE gaps) and the BAE accumulation point [9] which aligns well with the top of the beta-induced gap in the Alfvén continuum [44] or at the bottom of the TAE gaps. Note that higher frequency gaps (EAE, NAE, ... [2]) are not showed here to avoid overwhelming Fig. 12. We also indicate the MHD BAAE frequency from Eq. (3) which is located in the middle of the BAAE gaps predicted by the ALCON code. Note that such MHD continuum does not include ion drift effects so we do not expect to see a gap from drift and Alfvén/sound branches' coupling corresponding to a BTG mode. For consistency we also indicate the thermal ion diamagnetic frequency. The experimental estimation of the plasma frame frequency range of the observed EM perturbations is indicated by the shaded horizontal grey area, which includes the thermal ion diamagnetic frequency but excludes the MHD BAE and BAAE frequencies.

Having similar mode locations for BTG and BAE/BAAE modes makes the identification of modes from global linear gyrokinetic simulations challenging. In Section 4.2.1 and Section 4.2.2 we present our effort to clearly identify predicted modes with the GTC code to be BTG mode and not MHD BAE or BAAE mode.

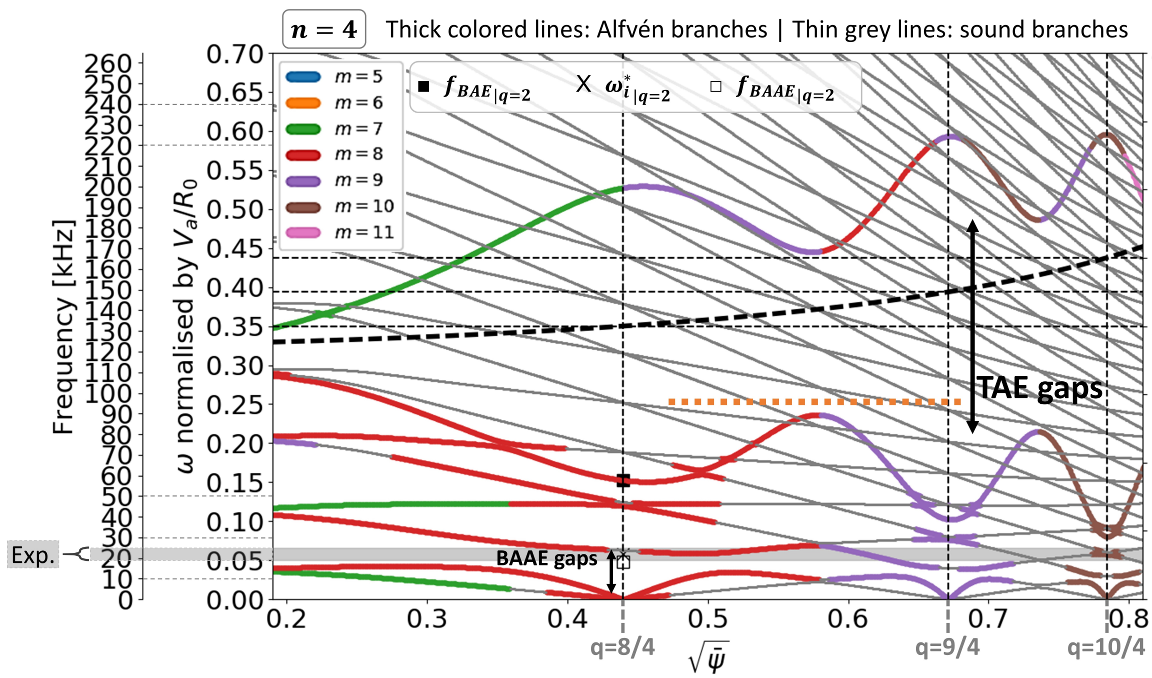

Figure 12: ALCON code [42] - Alfvén and sound continua of JET 92054 at 6.4s, solved for $n = 4$, $m \in [-20, 50]$, 2000 radial points ($\sqrt{\bar{\psi}} \in [0.01, 1.0]$). The thick colored lines are the Alfvén branches while the thin grey ones are the sound branches. The bold dashed line shows the q profile, thin vertical ones mark rational surfaces $q = 8/4 = 2$, $q = 9/4$ and $q = 10/4$. At $q = 2$, we indicate the characteristic plasma frame frequency for MHD BAE (full black square) and BAAE (empty black square) along with the thermal ion diamagnetic frequency (black cross). The orange horizontal dotted line at $\omega/\omega_0 \sim 0.25$ in the ($m = 8, m = 9$) TAE gap indicates the TAE predicted by the GTC code (Fig. 11). Note that the difference between ω/ω_0 with Fig. 10 is due to the different definition of the effective pressure between ALCON and CSCAS codes.

To study β effects we perform full non-perturbative calculations with the GTC code. We input thermal ion temperature and density profiles (Fig. 2) extracted from TRANSP code simulations. The thermal ion population is described by an initial Maxwellian distribution while the thermal electrons are treated as a massless fluid without kinetic effects. Some simulations have been run with electron kinetic effects included but only a marginal difference was found.

4.2.1. GTC, beta-induced modes in an uniform thermal plasma

Our first step is to use a synthetic antenna in GTC to scan in frequency the linear gyrokinetic response of the uniform thermal plasma (uniform density and temperature); Using a uniform plasma does not allow us to see any thermal plasma inhomogeneity effects, such as temperature gradient effects, but allows us to probe resonance conditions between plasma eigenmodes and an external perturbation. We use the experimental densities and temperatures at the $q = 2$ position to set the values of the uniform densities and temperatures. The antenna is set at a fixed frequency ($f_{antenna}$) and by running multiple simulations we can perform a frequency scan probing the different eigenmodes at various frequencies. Such GTC simulations impose an antenna field or excitation in the plasma at a certain radial location over a set radial range. The GTC synthetic antenna can be a perturbation of the electrostatic potential ($\delta\phi_{ant}$) or the parallel vector potential ($\delta A_{\|,ant}$). The latter has been used throughout this work since we are looking at electromagnetic modes. The GTC synthetic antenna has been modeled with Eq. (11) where $A(\psi)$ is a Gaussian envelope peaking at the location of the mode of interest (at the $q = 2$ magnetic surface in our simulations), ψ is the poloidal magnetic flux, θ is the poloidal angle and ζ is the toroidal angle.

$$A_{\|,ant} = A(\psi)\ cos(m\theta - n\zeta)\ cos(\omega t) \tag{11}$$

For each simulation, we then (a) calculate the power spectrum using a Fourier transform of the temporal evolution of the electrostatic potential of the ($n = 4,\ m = 8$) harmonic, and (b) extract from the power spectrum the maximum power around the input antenna frequency index. Looping for each simulation we get the linear gyrokinetic response of the thermal plasma over frequency in Fig. 13, i.e. how effectively the plasma resonates with the synthetic antenna perturbation at $f_{antenna}$. A peak in such a frequency scan indicates a sharper resonance condition. This method can also be used to quantify the damping rate of modes by fitting a peak with a cavity resonance function [29] or similarly appropriate resonance transfer function (TF) such as a weakly-damped harmonic oscillator TF.

We performed two frequency scans: (1) with the *low-*T_i profile and (2) with the *high-*T_i profile (see Fig. 2 for the profiles). Figure 13 shows the results from scan (1) which has a higher resolution with 22 simulations compared to 21 in the scan (2); one can see two peaks, one at $\omega/\omega_0 \sim 0.021$ below the MHD BAAE frequency and a second one at $\omega/\omega_0 \sim 0.185$ above the GAM/BAE frequency. The resonance around $\omega/\omega_0 \sim 0.021$ is identified as a BAAE mode heavily damped by ion Landau damping which is consistent with a recent

BAAE mode study using GTC [45] where $T_i \sim T_e$: a BAAE is found to be heavily damped by the thermal ions in similar simulations with an antenna excitation. The frequency of our predicted BAAE mode is too low compared to our experimental EM perturbations. The resonance around $\omega/\omega_0 \sim 0.185 \sim 1.95 v_i/R_0$ with $v_i = \sqrt{2T_i/m_i}$ is identified as a BAE mode weakly damped by ion transit resonance. The antenna scan peaks at about 21% above the Alfvén accumulation point frequency ($f_{GAM} \sim 1.61 v_i/R_0$). Such results are consistent with GTC simulations [46] studying damped BAEs excited by a synthetic antenna in toroidal plasmas with high safety factor ($q \in \{2, 3\}$).
With scan (2) we also find similar BAAE and BAE resonances. The BAAE one has a broader width meaning a higher damping, this is expected since T_i/T_e increase from scan (1, *low*-T_i) to scan (2, *high*-T_i), favouring the condition for the large ion Landau damping.
On both scans, there is no clear resonance near the ion diamagnetic frequency (ω_i^*) for BTG mode. No resonance associated with BTG mode is expected since such a non-perturbative mode is driven by the thermal ion temperature gradient so we need to consider thermal plasma inhomogeneity in our gyrokinetic simulations to capture diamagnetic effects.

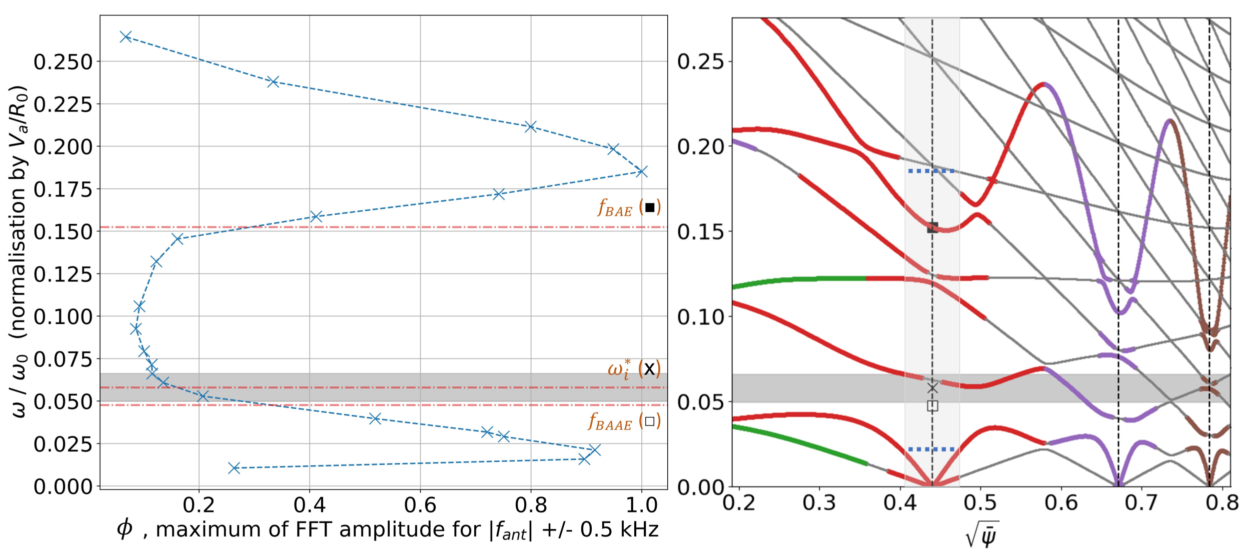

Figure 13: (left) GTC antenna frequency scan using the *low*-T_i profile; each cross corresponds to a single simulation. The different simulations are identical except for the antenna perturbation frequency. A peak in frequency indicates a resonant condition between plasma eigenmode and the antenna external perturbation. The peak around $\omega/\omega_0 \sim 0.021$ corresponds to BAAE mode while the peak around $\omega/\omega_0 \sim 0.185$ is identified as a BAE mode. (right) Alfvén-acoustic continuum (same as Fig. 12) zoomed in the sub-TAE frequency range. One can see a BAAE gap with the MHD BAAE frequency (f_{BAAE}, empty black square) in the middle while the frequency of the simulated BAAE mode is indicated by the dotted horizontal blue line at the bottom of this gap. The simulated BAE mode is indicated by the second dotted horizontal blue line above the Alfvén accumulation point frequency (full black square). The shaded horizontal grey area shows the experimental estimation of the plasma frame frequency of the observed EM perturbations with the thermal ion diamagnetic frequency (black cross) in the middle: the simulated BAAE mode frequency is too low while the BAE mode frequency is too high. Also, there is no clear resonance for BTG non-perturbative mode.

4.2.2. GTC, beta-induced modes in a non-uniform thermal plasma

We now perform self-consistent simulations with non-uniform density and temperature, where we find a physical mode kinetically driven by the thermal plasma, without fast ions, at $\omega/\omega_0 \sim 0.110$. Note that such a simulation with the initial value code picks up the fastest growing modes and only allows us to clearly identify the dominant driven mode, obscuring other damped/driven modes. Future work will explore the possibility to get a spectrum of modes along with their respective stability including damped modes. Figure 14 shows the characteristics of this $n = 4$ mode with a dominant $m = 8$ $(= nq = 4 * 2)$ poloidal harmonic with (a) the temporal evolution of the real and imaginary components of the mode's electrostatic potential ϕ and its amplitude $\|\phi\| = \sqrt{{\phi_r}^2 + {\phi_i}^2}$). (b) is the radial mode structure while (c) is the mode structure in the poloidal plane. From (a) one can see an exponential growth of the mode amplitude, we calculate the mode linear normalised growth rate ($\gamma/\omega \sim 23.8\%$) by fitting the linear growth of $log(\|\phi\|)$. Such a large linear growth rate is associated to a broad wave-particle resonance with direct energy exchange between the thermal plasma population and the mode as discussed below (Fig. 19).

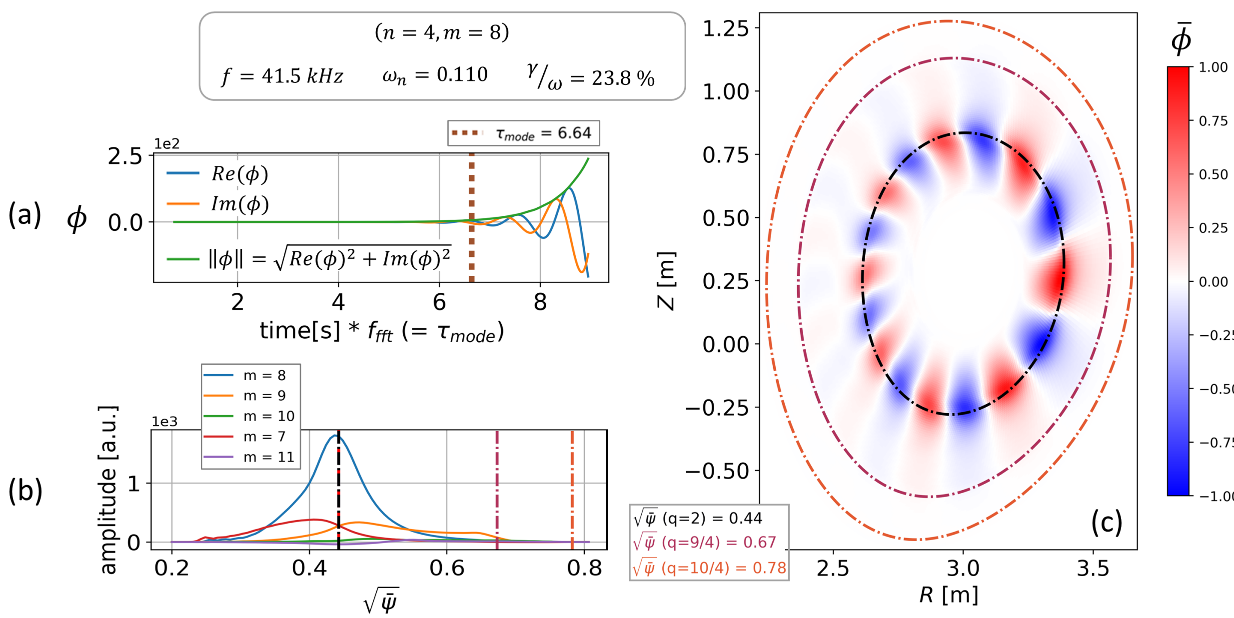

Figure 14: Time history for the mode ($n = 4$, $m = 8$); (a) blue and orange lines are respectively Real and Imaginary components of the electrostatic potential (ϕ) while green is the amplitude ($\sqrt{{\phi_r}^2 + {\phi_i}^2}$) which grows exponentially ($\gamma/\omega = 23.8\%$). (b) is the radial mode structure of the kinetically driven mode with $m = 8$ the dominant poloidal harmonic. (c) is the mode structure in the poloidal plane.

This kinetically driven mode matches well the experimental observations and theoretical predictions of BTG mode, i.e. is localised at the $q = 2$ magnetic surface, is dominated by a single poloidal harmonic, is driven by thermal ions and is moving in the ion diamagnetic direction. Its frequency, $\sim 41.5kHz \sim 0.110[V_A/R_0]$, is however between the ion diamagnetic

frequency and the BAE frequency. It's higher than expected from the experimental estimation by $\sim 15kHz$ (Section 2.2); such discrepancy is associated with the large growth rate of $\gamma \sim 10kHz$ and uncertainties on the thermal ion temperature profile and its gradient. Below we explore the nature of this kinetically driven mode to clearly distinguish between BTG and BAE modes.
We perform a toroidal mode number scan ($n \in [\![1, 6]\!]$); BAE modes should have similar frequencies in the plasma frame (or simulated frequency) while BTG modes would have different frequencies shifted by ω_i^*. The poloidal mode numbers were changed to model modes around the $q = 2$ surface similar to the $n = 4$ reference case: we used $m = nq + [-1, 0, +1, +2, +3]$. Figure 15 presents the mode frequency (kHz) and normalised growth rate (%) for each simulation. Not shown here to avoid overfilling the paper, the mode structures are very similar with a dominant single $m = nq$ poloidal harmonic as one can see on Fig. 14. We have a significant frequency dependency on the toroidal mode number: $\Delta f \sim 5kHz$ for n to $n \pm 1$, i.e. $\Delta f / f > 10\%$. This Δf corresponds to the ion diamagnetic frequency without n contribution from Eq. (1). These new results match what we expect from a drift-type mode, hence from a BTG mode.

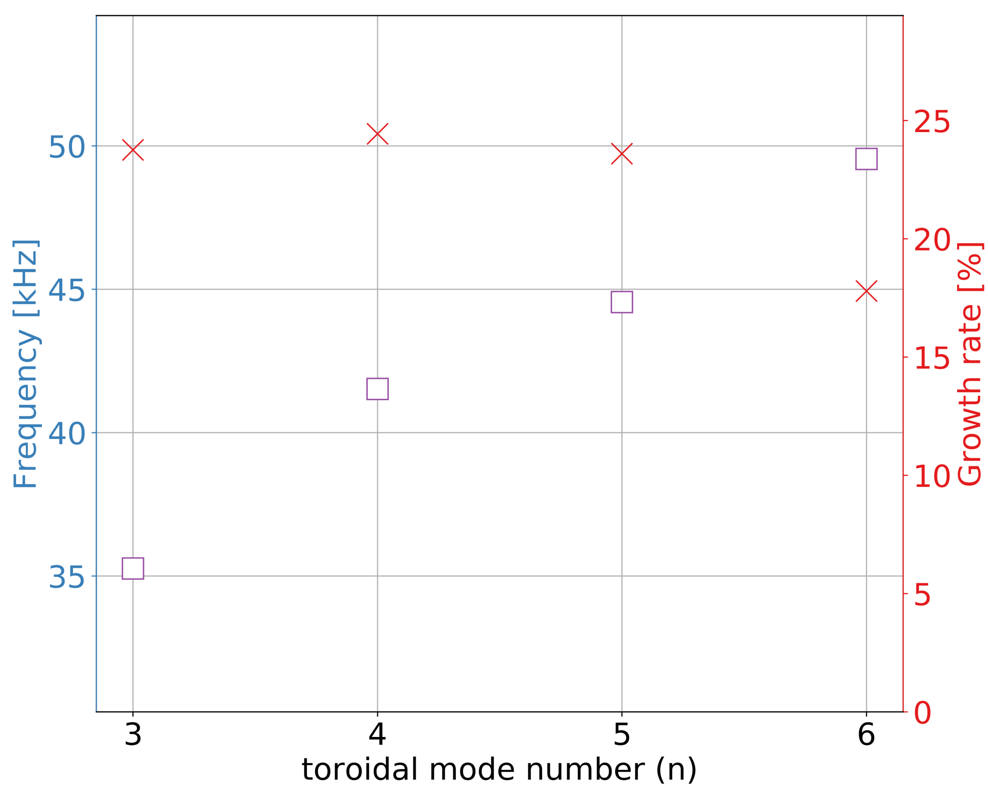

Figure 15: For $n \in [\![3, 6]\!]$: frequency (square) and normalised growth rate (cross) of the mode for each toroidal mode number. We note a clear mode frequency dependency on the toroidal mode number.

Now to confirm the effect of the thermal ion population on the drive of our reference mode, we perform a T_i scan while keeping the total plasma beta constant, i.e. if T_i is multiplied by a coefficient $A\%$ then T_e is multiplied by $(1-(A\%-1)T_i/T_e)$ since we use $n_e = n_i$ to respect quasi-neutrality. Note that $\nabla T_i/T_i$ remains the same. Figure 16 shows a clear effect of T_i on the stability of the mode; we can estimate a threshold from which the mode becomes unstable: $\sim 0.72 * T_i$. We also see little effect of T_i on the mode frequency indicating that the mode is affected by both thermal ions and electrons. This is confirmed by a second T_i scan for which we only vary T_i while keeping T_e constant: the threshold is $\sim 0.83 * T_i$ and the mode frequency slightly decreases with T_i/T_e increasing.

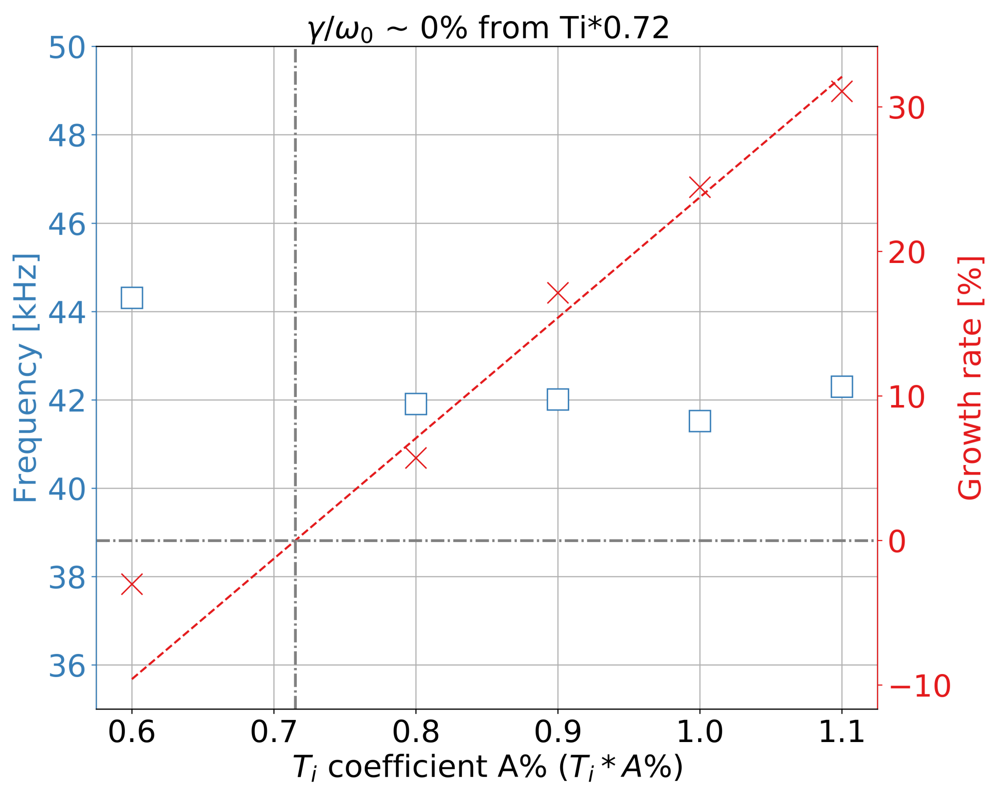

Figure 16: For $n = 4$, mode frequency (square) and normalised growth rate (cross) for several thermal plasma temperatures; when T_i is multiplied by a coefficient $A\%$, T_e is multiplied by $(1-(A\%-1)T_i/T_e)$. Clear effect from T_i on the stability of the reference mode. For simulations with driven mode $(0.72 * T_i \precsim T_i)$, the mode frequency is marginally affected by T_i.

To complement the analysis of our reference case, we also performed the following studies:

- Mode polarisation (details of the calculation can be found in [29]):
  - Electric field polarisation: we analyse the ratio between the parallel electric field and its electrostatic component $(E_\parallel/E_{\parallel,ES})$ defined by

$$\begin{aligned} E_\parallel &= -\mathbf{b_0}\cdot\nabla\delta\phi - \frac{1}{c}\frac{\partial \delta A_\parallel}{\partial t} \\ E_{\parallel,ES} &= -\mathbf{b_0}\cdot\nabla\delta\phi \end{aligned} \tag{12}$$

where $\mathbf{b_0}$ represents the equilibrium magnetic field direction, $\delta\phi$ is the electrostatic potential and $\delta A_\parallel$ is the parallel vector potential. $E_\parallel = 0$ for an ideal Alfvénic wave, and $E_\parallel = E_{\parallel,ES}$ for an electrostatic ion acoustic wave and drift wave. For our reference mode (Fig. 17) we get $E_\parallel/E_{\parallel,ES} \sim 0.1$ using volume-average of square of $E_\parallel$ and $E_{\parallel,ES}$ indicating a dominant Alfvénic character which is consistent with BTG theory [6].

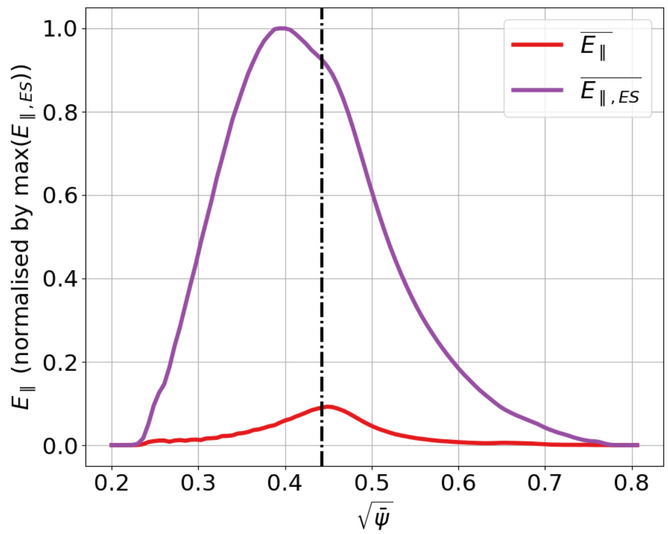

Figure 17: Reference mode's (Fig. 14) normalised radial profile of parallel electric field $E_\parallel$ and its electrostatic part $E_{\parallel,ES}$.

- Magnetic perturbation polarisation: we analyse the ratio between the parallel and perpendicular magnetic perturbations ($\delta B_\parallel/\delta B_\perp$). $\delta B_\parallel/\delta B_\perp = 0$ for a shear Alfvénic wave, and $\delta B_\parallel/\delta B_\perp$ is finite for slow magnetoacoustic and drift waves. For our reference mode (Fig. 18) we get $\delta B_\parallel/\delta B_\perp \sim 0.45$ using volume-average of square of $\delta B_\parallel$ and $\delta B_\perp$ confirming the nature of the mode being a coupling between Alfvén and drift waves.

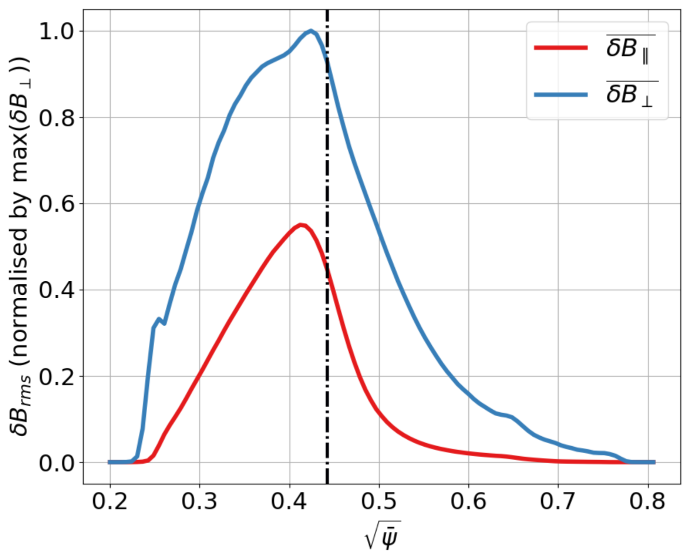

Figure 18: Reference mode's (Fig. 14) normalised radial profiles of flux surface-averaged perpendicular ($\delta B_\perp$) and parallel ($\delta B_\parallel$) perturbed magnetic field B_{rms}.

- Wave-particle energy exchange: we analyse the direct energy exchange between the thermal plasma and the wave/mode. We use the rate of work done on the thermal ion particles by the wave/mode to calculate the time rate of change of the wave/mode energy density (δW) [29, 37]:

$$\frac{\mathrm{d}\delta W}{\mathrm{d}t} = \langle -Ze\mathbf{v}_\perp \cdot \mathbf{E}_\perp - Ze\nu_\parallel E_\parallel \rangle \tag{13}$$

where Ze is the particle charge, $\mathbf{v}_\perp$ is the guiding center Grad-B ($\boldsymbol{v}_{\boldsymbol{\nabla B}}$) and curvature ($\boldsymbol{v}_{\boldsymbol{R}}$) drifts, $\mathbf{E}_\perp = -\nabla_\perp \delta\phi$ is the perpendicular electric field and $\nu_\parallel$ is the guiding center parallel velocity. The brackets denote a flux-surface averaging and a gyrocenter velocity space integral weighted by the perturbed distribution function. Note that both the perpendicular and parallel energy transfers include the non-resonant (fluid) as well as the resonant (kinetic) energy exchanges. The interchange drive represents only the fluid parts of the energy exchange rate. In Fig. 19 one can see that the perpendicular energy exchange is the source of the drive of the mode while the interchange drive is low, which indicates a dominant perpendicular energy transfer from the thermal ions to the mode coming mostly from the resonant (kinetic) energy exchange. This analysis confirms that the reference mode is kinetically driven by thermal ions and that such a mode differs from the DIII-D LFM identified as an interchange-like electromagnetic mode.

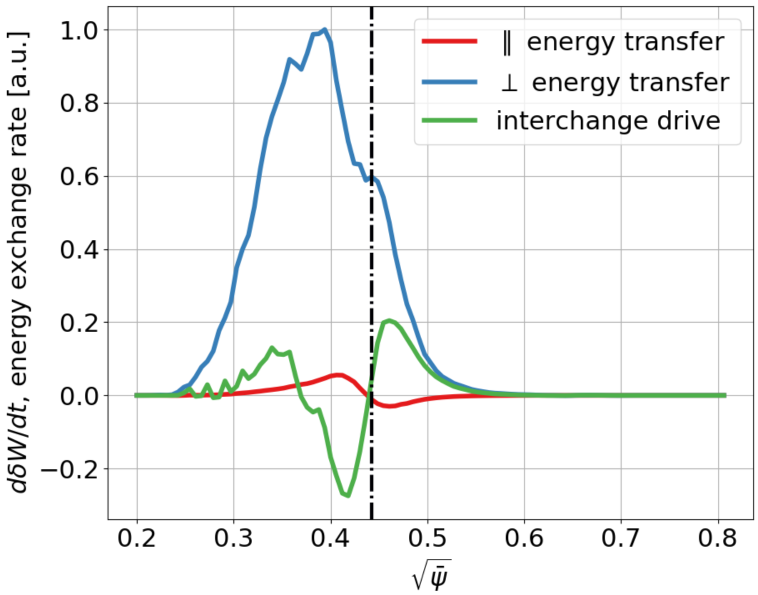

Figure 19: Reference mode's (Fig. 14) time rate of change of the wave/mode energy density. Normalised radial profiles of the parallel and perpendicular energy exchange rates as well as the interchange (non-resonant) part. The perpendicular energy transfer is the source of the drive of the wave/mode.

- Incompressible MHD simulation: reference mode was not found, so it confirms that our reference mode is not an interchange-type mode which is consistent with the wave-particle energy exchange analysis.
- Including kinetic effects from trapped electrons using a fluid-kinetic hybrid electron model [47] has an insignificant effect on the reference mode characteristics confirming the strong dependence of the reference mode on the thermal ion population.
- Electrostatic simulation with adiabatic electrons: reference mode was not found which indicates that our reference mode is not an electrostatic mode; this is consistent with the electromagnetic nature of the BTG modes.
- Without $\delta B_{\|}$ we see similar characteristics of the reference mode but with a significant reduction of its growth rate indicating an important effect from $\delta B_{\|}$ often neglected in gyrokinetic simulations.

Many features in our reference case obtained with GTC are therefore consistent with experimental observations and analytical theories of beta-induced ion temperature gradient driven eigenmodes, i.e. a strong thermal ion dependence especially with the significant thermal ion temperature gradient; a propagation in the ion diamagnetic direction; a localisation near a rational magnetic surface ($q = 2$) with a low magnetic shear; a coupling among Alfvén and drift waves with a dominant Alfvénic polarisation; a single dominant poloidal harmonic and a frequency scaling with the ion diamagnetic frequency. The simulated mode frequency is however over-estimated by $\sim 15kHz$ compare to the frequency estimated from the experiment ($f_{GTC} \sim 41.5kHz \sim 0.110[V_A/R_0]$ compared to the expected EM modes estimated to be around $\omega^*_{i\,|n=4} \sim 21.9 \pm 3.1kHz \sim 0.059[V_A/R_0]$ from the experiment). A few factors can contribute to such uncertainty: the large growth rate of the simulated mode ($\gamma \sim 10kHz$), the uncertainties on the thermal ion temperature measurements/profiles as stressed by Fig. 2 and its (very) high ion-temperature gradient, the GTC local Maxwellian distribution function used as an approximation to the neoclassical distribution function, and finally the measured Doppler shift frequency correction which neglects the neoclassical poloidal flows.

5. Summary

JET pulse #92054, a hot ion JET plasma with elevated monotonic q profile and clear ITB, exhibits unstable electromagnetic perturbations with frequencies below the TAE frequency which have been identified as beta-induced ion temperature gradient (BTG) eigenmodes. Experimental investigations show that the BTG modes have a strong dependence on the thermal ions, particularly on the thermal ion temperature gradient, are localised near the $q = 2$ magnetic surface related to the ITB and have a frequency that scales with the ion diamagnetic frequency (ω_i^*). These experimental characteristics are in good agreement with BTG mode analytical theories [32,33]. Such theories also predict three well-defined conditions for BTG mode to exist which are fullfilled by the JPN 92054 plasma; i.e. positive relative ion temperature gradient, ion beta higher than a critical value, a low magnetic shear and BTG mode analytical dispersion relation reducing to $Re(\omega) = \omega_i^*$. Ref. [33] predicts that a BTG mode is a coupling among Alfvén and drift waves as well as that it is driven by inverse ion Landau damping due to the high thermal ion temperature gradient. Many of these BTG mode experimental and theoretical features are consistent with gyrokinetic simulations using the code GTC [28] with a realistic magnetic geometry and plasma profiles: we find a mode kinetically driven by thermal ions localised near the $q = 2$ magnetic surface with a dominant Alfvénic polarisation and a frequency scaling with the ion diamagnetic frequency (ω_i^*).

BTG modes are also observed in *recent* JET plasmas during energetic particle scenario experiments aiming to study alpha driven AEs, performed in JET 2019/2020 Deuterium campaigns. Reflectometer diagnostic data with a better radial resolution than for JPN 92054 is available for some of these pulses and confirms the mode location being around the $q = 2$ magnetic surface. We also observe a correlation between the BTG modes stability and the neutron rate roll-over, but this study is beyond the scope of this work; it will be discussed in future publications.

Acknowledgments

The authors would like to thank Phillip Bonofiglo, Clive Challis, Jian Bao, Benjamin Chapman, Lorenzo Frassinetti, David Hatch, Christian Perez Von Thun, Anthony Field, Mykola Dreval, António Figueiredo and David Keeling for their helpful discussions regarding JET pulse #92054 analysis. Special thanks to the JET team - JET task force leaders, machine operators, diagnosticians, and others - for all the high quality data available.

This work has been carried out within the framework of the EUROfusion Consortium and has received funding from the Euratom research and training programme 2014-2018 and 2019-2020 under grant agreement No 633053 and from the RCUK [grant number EP/T012250/1]. The views and opinions expressed herein do not necessarily reflect those of the European Commission.

This work was supported by U.S. Department of Energy (DOE) through DEFG02-99ER54563 as well as DOE SciDAC project ISEP and used resources of the Oak Ridge

Leadership Computing Facility at Oak Ridge National Laboratory (DOE Contract No. DE-AC05-00OR22725) and the National Energy Research Scientific Computing Center (DOE Contract No. DE-AC02-05CH11231).

Data Availability

To obtain further information on the data and models underlying this paper please contact PublicationsManager@ukaea.uk. The data that support the findings of this study are also available from the corresponding author upon reasonable request.

References

[1] R. J. Dumont, J. Mailloux, V. Aslanyan, M. Baruzzo, C.D. Challis, I. Coffey, A. Czarnecka, E. Delabie, J. Eriksson, J. Faustin, J. Ferreira, M. Fitzgerald, J. Garcia, L. Giacomelli, C. Giroud, N. Hawkes, Ph. Jacquet, E. Joffrin, T. Johnson, D. Keeling, D. King, V. Kiptily, B. Lomanowski, E. Lerche, M. Mantsinen, L. Meneses, S. Menmuir, K. McClements, S. Moradi, F. Nabais, M. Nocente, A. Patel, H. Patten, P. Puglia, R. Scannell, S. Sharapov, E. R. Solano, M. Tsalas, P. Vallejos, H. Weisen, and JET Contributors. Scenario development for the observation of alpha-driven instabilities in JET DT plasmas. *Nuclear Fusion*, 58(8):082005, 2018.

[2] W. W. Heidbrink. Basic physics of Alfvén instabilities driven by energetic particles in toroidally confined plasmas. *Physics of Plasmas*, 15(5):055501, 2008.

[3] W. W. Heidbrink, E. J. Strait, M. S. Chu, and A. D. Turnbull. Observation of Beta-Induced Alfvén Eigenmodes in the DIII-D Tokamak. *Physics Review Letters*, 71(6):855–858, 1993.

[4] A. D. Turnbull, E. J. Strait, W. W. Heidbrink, M. S. Chu, H. H. Duong, J. M. Greene, L. L. Lao, T. S. Taylor, and S. J. Thompson. Global Alfvén modes: Theory and experiment*. *Physics of Fluids B: Plasma Physics*, 5:2546–2553, 1993.

[5] N.N. Gorelenkov, H.L. Berk, E. Fredrickson, S.E. Sharapov, and JET EFDA Contributors. Predictions and observations of low-shear beta-induced shear Alfvén–acoustic eigenmodes in toroidal plasmas. *Physics Letters A*, 370:70–77, 2007.

[6] A. B. Mikhailovskii and S. E. Sharapov. Beta-induced Temperature-gradient Eigenmodes in Tokamaks. *Plasma Physics Report*, 25:911, 1999.

[7] J. Wesson. *Tokamaks*. Clarendon Press-Oxford, 3rd edition, 2004.

[8] F. Romanelli. Ion temperature-gradient-driven modes and anomalous ion transport in tokamaks. *Physics of Fluids B: Plasma Physics*, 1:1018, 1989.

[9] F. Zonca, L. Chen, and R. A. Santoro. Kinetic theory of low-frequency Alfvén modes in tokamaks. *Plasma Phys. Control. Fusion*, 38:2011–2028, 1996.

[10] F. Zonca, L. Chen, R. A. Santoro, and J. Q. Dong. Existence of discrete modes in an unstable shear Alfvén continuous spectrum. *Plasma Phys. Control. Fusion*, 40:2009–2021, 1998.

[11] F. Zonca, L. Chen, J. Q. Dong, and R. A. Santoro. Existence of ion temperature gradient driven shear Alfvén instabilities in tokamaks. *Physics of Plasmas*, 6:1917–1924, 1999.

[12] S.T. Tsai and L. Chen. Theory of kinetic ballooning modes excited by energetic particles in tokamaks. *Physics of Fluids B: Plasma Physics*, 5:3284–3290, 1993.

[13] C. Z. Cheng. Kinetic theory of collisionless ballooning modes. *The Physics of Fluids*, 25:1020, 1982.

[14] P. Puglia, W. Pires De Sa, P. Blanchard, S. Dorling, S. Dowson, A. Fasoli, J. Figueiredo, R. Galvão, M. Graham, G. Jones, C. Perez Von Thun, M. Porkolab, L. Ruchko, D. Testa, P. Woskov, and M. A. Albarracin-Manrique. The upgraded JET toroidal Alfvén eigenmode diagnostic system. *Nuclear Fusion*, 56(11), 2016.

[15] R. A. Tinguely, P. G. Puglia, N. Fil, S. Dowson, M. Porkolab, A. Fasoli, D. Testa, and JET Contributors. Results from the Alfvén Eigenmode Active Diagnostic during the 2019-2020 JET deuterium campaign. *Plasma Physics and Controlled Fusion*, 62(11):115002, 2020.

[16] M. Baruzzo, B. Alper, T. Bolzonella, M. Brix, P. Buratti, C. D. Challis, F. Crisanti, E. de la Luna, P. C. de Vries, C. Giroud, N. C. Hawkes, D. F. Howell, F. Imbeaux, E. Joffrin, H. R. Koslowski, X. Litaudon, J. Mailloux, A. C. C. Sips, O. Tudisco, and JET contributors. Neoclassical tearing mode (NTM) magnetic spectrum and magnetic coupling in JET tokamak. *Plasma Phys. Control. Fusion*, 52:075001, 2010.

[17] L.L. Lao, H. St. John, R.D. Stambaugh, A.G. Kellman, and W. Pfeiffer. Reconstruction of current profile parameters and plasma shapes in tokamaks. *Nuclear Fusion*, 25(11):1611–1622, 1985.

[18] R. J. Goldston, D. C. McCune, H. H. Towner, S. L. Davis, R. J. Hawryluk, and G. L. Schmidt. New techniques for calculating heat and particle source rates due to neutral beam injection in axisymmetric tokamaks. *Journal of Computational Physics*, 43:61–78, September 1981.

[19] C.D. Challis, J. Garcia, M. Beurskens, P. Buratti, E. Delabie, P. Drewelow, L. Frassinetti, C. Giroud, N. Hawkes, J. Hobirk, E. Joffrin, D. Keeling, D.B. King, C.F. Maggi, J. Mailloux, C. Marchetto, D. McDonald, I. Nunes, G. Pucella, S. Saarelma, J. Simpson, and JET Contributors. Improved confinement in JET high β plasmas with an ITER-like wall. *Nuclear Fusion*, 55:053031, 2015.

[20] L. Garzotti, C.D. Challis, R. Dumont, D. Frigione, J. Graves, E. Lerche, J. Mailloux, M. Mantsinen, F. Rimini, F. Casson, A. Czarnecka, J. Eriksson, R. Felton, L. Frassinetti, D. Gallart, J. Garcia, C. Giroud, E. Joffrin, Hyun-Tae Kim, N. Krawczyk, M. Lennholm, P. Lomas, C. Lowry, L. Meneses, I. Nunes, C.M. Roach, M. Romanelli, S. Sharapov, S. Silburn, A. Sips, E. Stefániková, M. Tsalas, D. Valcarcel, M. Valovič, and JET Contributors. Scenario development for D–T operation at JET. *Nuclear Fusion*, 59(7):076037, 2019.

[21] T.C. Luce, C.D. Challis, S. Ide, E. Joffrin, Y. Kamada, P.A. Politzer, J. Schweinzer, A.C.C. Sips, J. Stober, G. Giruzzi, C.E. Kessel, M. Murakami, Y.-S. Na, J.M. Park, A.R. Polevoi, R.V. Budny, J. Citrin, J. Garcia, N. Hayashi, J. Hobirk, B.F. Hudson, F. Imbeaux, A. Isayama, D.C. McDonald, T. Nakano, N. Oyama, V.V. Parail, T.W. Petrie, C.C. Petty, T. Suzuki, M.R. Wade, the ITPA Integrated Operation Scenario Topical Group Members, the ASDEX-Upgrade Team, the DIII-D Team, JET EFDA Contributors, and the JT-60U Team. Development of advanced inductive scenarios for ITER. *Nuclear Fusion*, 54:013015, 2013.

[22] E. Joffrin, M. Baruzzo, M. Beurskens, C. Bourdelle, J. Bucalossi S. Brezinsek4, P. Buratti, G. Calabro, C.D. Challis, M. Clever, J. Coenen, E. Delabie, R. Dux, P. Lomas, E. de la Luna, P. de Vries, J. Flanagan, L. Frassinetti, D. Frigione, C. Giroud, M. Groth, N. Hawkes, J. Hobirk, M. Lehnen, G. Maddison, J. Mailloux, C.F. Maggi, G. Matthews, M. Mayoral, A. Meigs, R. Neu, I. Nunes, T. Puetterich, F. Rimini, M. Sertoli, B. Sieglin, A.C.C. Sips, G. van Rooij, I. Voitsekhovitch, , and JET-EFDA Contributors. First scenario development with the JET new ITER-like wall. *Nuclear Fusion*, 54:013011, 2014.

[23] H.J.C. Oliver, S.E. Sharapov, B.N. Breizman, A.K. Fontanilla, D.A. Spong, D. Terranova, and JET contributors. MHD spectroscopy of JET plasmas with pellets via Alfvén eigenmodes. *Nuclear Fusion*, 59:1–14, September 2019.

[24] R. J. Hastie, P. J. Catto, , and J. J. Ramos. Effect of strong radial variation of the ion diamagnetic frequency on internal ballooning modes. *Physics of Plasmas*, 7(11):4561, 2000.

[25] M.A. Van Zeeland, W.W. Heidbrink, S.E. Sharapov, D. Spong, A. Cappa, Xi Chen, C. Collins, M. García-Muñoz, N.N. Gorelenkov, G.J. Kramer, P. Lauber, Z. Lin, and C. Petty. Electron cyclotron heating can drastically alter reversed shear Alfvén eigenmode activity in DIII-D through finite pressure effects. *Nuclear Fusion*, 56:112007, 2016.

[26] W. W. Heidbrink, M.A. Van Zeeland, M.E. Austin, A. Bierwage, L. Chen, G.J. Choi, P. Lauber, Z. Lin, G.R. McKee, and D.A. Spong. 'BAAE' instabilities observed without fast ion drive. *Nuclear Fusion*, 61:016029, 2021.

[27] N. N. Gorelenkov, M. A. Van Zeeland, H. L. Berk, N. A. Crocker, D. Darrow, E. Fredrickson, G.-Y. Fu,

W. W. Heidbrink, J. Menard, and R. Nazikian. Beta-induced Alfvén-acoustic eigenmodes in National Spherical Torus Experiment and DIII-D driven by beam ions. *Physics of Plasmas*, 16:056107, 2009.

[28] Z. Lin, T. S. Hahm, W. W. Lee, W. M. Tang, and R. B. White. Turbulent Transport Reduction by Zonal Flows: Massively Parallel Simulations. *Science*, 281:1835–1837, 1998.

[29] G.J. Choi, P. Liu, X.S. Wei, J.H. Nicolau, G. Dong, W.L. Zhang, Z. Lin, W.W. Heidbrink, and T.S. Hahm. Gyrokinetic simulation of low-frequency Alfvénic modes in DIII-D tokamak. *Nuclear Fusion*, 61:066007, 2021.

[30] D. Freedman, R. Pisani, and R. Purves. Statistics. *4th edition. WW Norton & Company, New York*, 2007.

[31] W. W. Heidbrink. What is the "beta-induced Alfvén eigenmode?". *Physics of Plasmas*, 6(4):1147, 1999.

[32] A. B. Mikhailovskii and S. E. Sharapov. Beta-induced Temperature-gradient Eigenmodes in Tokamaks. MHD Theory. *JET Joint Undertaking Reports*, JET–P(98)18:1–22, 1998.

[33] A. B. Mikhailovskii and S. E. Sharapov. Beta-induced Temperature-gradient Eigenmodes in Tokamaks. Kinetic Theory. *JET Joint Undertaking Reports*, JET–P(98)12:1–16, 1998.

[34] A. B. Mikhailovskii. "Drift" instabilities distorting the magnetic surfaces of Tokamak-type toroidal systems. *Nuclear Fusion*, 13:259, 1973.

[35] A. B. Mikhailovskii, G. T. A. Huysmans, W. O. K. Kerner, and S. E. Sharapov. Optimization of computational MHD normal-mode analysis for tokamaks. *Plasma Physics Reports*, 23(10):844–857, 1997.

[36] S. Taimourzadeh, E.M. Bass, Y. Chen, C. Collins, N.N. Gorelenkov, A. Könies, Z.X. Lu, D.A. Spong, Y. Todo, M.E. Austin, J. Bao, A. Biancalani, M. Borchardt, A. Bottino, W.W. Heidbrink, R. Kleiber, Z. Lin, A. Mishchenko, L. Shi, J. Varela, R.E. Waltz, G. Yu, W.L. Zhang, , and Y. Zhu. Verification and validation of integrated simulation of energetic particles in fusion plasmas. *Nuclear Fusion*, 59:066006, 2019.

[37] Y. Liu, Z. Lin, H. Zhang, and W. Zhang. Excitation of low frequency Alfvén eigenmodes in toroidal plasmas. *Nuclear Fusion*, 57:114001, 2017.

[38] G.T.A. Huysmans, J.P. Goedbloed, and W. Kerner. Isoparametric Bicubic Hermite Elements for Solution of the Grad-Shafranov Equation. *International Journal of Modern Physics C*, 02(01):371–376, 1991.

[39] G. T. A. Huysmans, S. E. Sharapov, A. B. Mikhailovskii, and W. Kerner. Modeling of diamagnetic stabilization of ideal magnetohydrodynamic instabilities associated with the transport barrier. *Physics of Plasmas*, 8(10):4292–4305, 2001.

[40] R. B. White and M. S. Chance. Hamiltonian guiding center drift orbit calculation for plasmas of arbitrary cross section. *The Physics of Fluids*, 27:2455–2467, 1984.

[41] I. Holod, W. L. Zhang, Y. Xiao, and Z. Lin. Electromagnetic formulation of global gyrokinetic particle simulation in toroidal geometry. *Physics of Plasmas*, 16:122307, 2009.

[42] W. Deng, Z. Lin, I. Holod, Z. Wang, Y. Xiao, and H. Zhang. Linear properties of reversed shear Alfvén eigenmodes in the DIII-D tokamak. *Nuclear Fusion*, 52:043006, 2012.

[43] C. Z. Cheng and M. S. Chance. Low-n shear Alfvén spectra in axisymmetric toroidal plasmas. *The Physics of Fluids*, 29:3695, 1986.

[44] M. S. Chu, J. M. Greene, L. L. Lao, A. D. Turnbull, and M. S. Chance. A numerical study of the high-n shear Alfvén spectrum gap and the high-n gap mode. *Physics of Fluids B: Plasma Physics*, 4:3713, 1992.

[45] H. S. Zhang, Y. Q. Liu, Z. Lin, and W. L. Zhang. Gyrokinetic particle simulation of beta-induced Alfvén-acoustic eigenmode. *Physics of Plasmas*, 23:042510, 2016.

[46] H. S. Zhang, Z. Lin an I. Holod, Y. Xiao, and W. L. Zhang. Gyrokinetic particle simulation of beta-induced Alfvén eigenmode. *Physics of Plasmas*, 17:112505, 2010.

[47] Z. Lin and L. Chen. A Fluid-Kinetic Hybrid Electron Model for Electromagnetic Simulations. *Physics of Plasmas*, 8:1447, 2001.